

The effects of varying depth in cosmic shear surveys

Sven Heydenreich

Masterarbeit in Physik
angefertigt im Argelander-Institut für Astronomie

vorgelegt der
Mathematisch-Naturwissenschaftlichen Fakultät
der
Rheinischen Friedrich-Wilhelms-Universität
Bonn

March 2019

I hereby declare that this thesis was formulated by myself and that no sources or tools other than those cited were used.

Bonn,
Date

.....
Signature

1. Gutachter: Prof. Dr. Peter Schneider
2. Gutachter: Prof. Dr. Hendrik Hildebrandt

Acknowledgements

I would like to thank my supervisors, Peter Schneider and Hendrik Hildebrandt, for countless hints, tips, remarks and helpful discussions on a broad range of topics, regarding both the content and the presentation of this thesis. Furthermore I would like to thank Patrick Simon for helpful insights in the numerical calculation of shear correlation functions. I would like to thank Sandra Unruh for reading this work, offering many crucial remarks as well as insightful discussions, and for the creation of Figures [2.1](#) and [2.2](#). Additionally I would like to thank Jan Luca van den Busch for his permission to use and modify his code for a Markov-Chain-Monte-Carlo simulation.

Last but not least, I would like to thank my family for their undying support; without that I would not have been able to choose this path.

Abstract

Cosmic shear proves to be a powerful tool to study the properties of the local Universe. This method is especially sensitive to the parameter $S_8 = \sigma_8 \sqrt{\Omega_m/0.3}$. Most current cosmic shear analyses determine a value of S_8 that is significantly lower than the one determined by analysis of the Cosmic Microwave Background by the Planck Collaboration. This might be a statistical coincidence, a sign for the incompleteness of the standard model or the consequence of a systematic effect that has not yet been accounted for. One systematic effect for ground-based surveys is imposed by a change in atmospheric conditions between pointings, which leads to a variation in depth. We want to understand and quantify the resulting effects. A convenient check for remaining systematics is the analysis of B-modes, which to leading order cannot be created by astrophysical phenomena. We investigate if a variation in depth introduces a bias to the cosmological parameters and whether it can be responsible for the creation of B-modes. We construct a semi-analytic model to estimate the impact on the shear correlation functions and analyze the implications for cosmological parameters in a Markov-Chain-Monte-Carlo simulation. Furthermore, we construct Complete Orthogonal Sets of E- and B-mode Integrals (COSEBIs) of the correlation functions to quantify the occurring B-modes. For the Kilo-Degree Survey, this effect introduces an error in ξ_{\pm} of the order of a few percent on small scales, which is responsible for a 0.1σ bias in Ω_m and σ_8 . However, the parameter S_8 is robust against this modification. We also report the occurrence of B-modes, although not to a degree that would be significant in current surveys. We conclude that the effects of varying depth on cosmological parameters are not yet significant, but have to be accounted for in next-generation experiments like Euclid.

Contents

1	Introduction	1
2	Theoretical background	3
2.1	Cosmology	3
2.1.1	The standard model of cosmology	3
2.1.2	Distances in cosmology	5
2.1.3	Structure growth	6
2.2	Gravitational lensing	9
2.2.1	Theoretical framework	9
2.2.2	Weak lensing and cosmic shear	11
2.2.3	Separating E- and B-modes in gravitational lensing	15
3	The effects of varying depth	19
3.1	Toy model – a single lens plane	21
3.1.1	Modelling a shear field	22
3.1.2	Effects on the power spectrum	22
3.1.3	The function $E(\theta)$	24
3.1.4	Modelling the shear correlation functions	26
3.2	Semi-analytical model for the shear correlation functions	28
4	Results	31
5	Discussion and conclusion	35
	Bibliography	37
A	Detailed calculations	39
A.1	Calculation of the power spectrum	39
A.2	Calculation of the shear correlation functions	41
B	Outlook: Finite field effects	43
C	Additional figures and fables	47
C.1	Additional tables	47
C.2	Results of the MCMC	48
C.3	Finite field effects	50
	List of Figures	53
	List of Tables	55

Introduction

For the last two decades, the Λ CDM model has been the standard model of cosmology. With only a few free parameters, it is able to explain a huge variety of observations; the existence and fluctuations of the Cosmic Microwave Background (CMB), the large scale structure in the Universe, the luminosity of supernovae of type Ia and the abundances of light elements all yield roughly consistent results for the standard model. Apart from the nature of Dark Matter and Dark Energy, the challenges for modern cosmology are the precise determination of the free parameters as well as the search for possible extensions to the standard model.

One tool to probe the Λ CDM Model and determine its parameters was provided by the discovery of cosmic shear: The distortion of light bundles travelling from distant galaxies through the matter distribution of the Universe to Earth provides useful insights on the large scale structure. Contrary to the analysis of the CMB by Planck Collaboration et al. (2018), cosmic shear is more sensitive to the properties of the local Universe and thus provides an excellent consistency check for the standard model of cosmology. Current cosmic shear surveys are especially sensitive to the parameter $S_8 = \sigma_8 \sqrt{\Omega_m/0.3}$, where σ_8 denotes the normalisation of the matter power spectrum and Ω_m is the matter density. It is interesting to note that all three current major cosmic shear results report a lower S_8 than inferred from CMB analysis: While Planck Collaboration et al. (2018) determined a value of $S_8 = 0.830 \pm 0.013$, Hikage et al. (2019) report $S_8 = 0.800^{+0.029}_{-0.028}$ from analysis of the Subaru Hyper Suprime-Cam survey, Hildebrandt et al. (2018) report $0.737^{+0.040}_{-0.036}$ from KiDS+VIKING data and the Dark Energy Survey (Troxel et al. 2018) reports $S_8 = 0.782 \pm 0.027$. Also, Heymans et al. (2013) report $S_8 = 0.759 \pm 0.020$ from analysis of CFHTLenS data. This discrepancy has received a lot of attention (Verde, Protopapas and Jimenez 2013). It could be interpreted as a statistical coincidence, a sign of new physics like massive neutrinos (Battye and Moss 2014), time-varying dark energy or modified gravity (Planck Collaboration et al. 2016); or as the manifestation of a systematic effect, either in the cosmic shear surveys or in the Planck mission (Addison et al. 2016), that is not yet accounted for.

As weak gravitational lensing measures a tiny signal over a large sample, it is extremely sensitive to anything that systematically biases the measurements, such that the error bars in current surveys arise to equal parts from statistical and systematic uncertainties (compare Hildebrandt et al. 2017). With next-generation surveys like the Large Synoptic Survey Telescope and Euclid right at the doorstep, systematic effects in gravitational lensing have received an unprecedented amount of attention (Asgari et al. 2018; Blake 2019; Shirasaki et al. 2019).

To check for remaining systematics, a weak lensing signal can be divided into two components, the so-called E- and B-modes (Crittenden et al. 2002; Schneider, van Waerbeke and Mellier 2002). To leading order, B-modes can not be created by astrophysical phenomena and are thus an excellent test

for remaining systematics. As Hildebrandt et al. (2017) reported the significant detection of B-modes, it was well motivated to check for possible systematics that are not yet accounted for. Note that the non-existence of B-modes does not necessarily imply that the sample is free of remaining systematics.

One systematic effect is the variation of depth in a survey. While effects like Galactic extinction or dithering strategies do play a role in every survey, this work focuses on the effects caused by varying atmospheric conditions, that are found in ground-based surveys. To first order, this variation can be modelled by a step-like depth function which varies from pointing to pointing. In this work we assume the specifications of the Kilo-Degree Survey, namely a collection of 1 deg^2 square fields.

We will give a brief overview over the necessary knowledge in cosmology and gravitational lensing in Chapter 2. We will then review the extent of the variation of depth in the KiDS+VIKING-450 survey in Chapter 3 and develop several models to describe its effect in Sections 3.1 and 3.2. Afterwards we will present our results in Chapter 4 and discuss them in Chapter 5, focussing on the used simplifications and possible mitigation strategies.

Theoretical background

In this chapter we will review the background knowledge in cosmology and gravitational lensing that is necessary to understand the contents of this thesis. This summary is mainly condensed from Bartelmann and Schneider (2001) and Schneider (2015), more detailed explanations can be found in these works. We will treat the standard model of cosmology, and go into a little more detail regarding the evolution of the large-scale structure. Afterwards, we will explain the basics of gravitational lensing and how to probe said large-scale structure using cosmic shear. A reader familiar with these topics can skip this chapter.

2.1 Cosmology

2.1.1 The standard model of cosmology

All observational evidence suggests that the Universe around us is *isotropic* on large scales. Assuming that our spatial position in the Universe is not special, and thus that the Universe is isotropic around all points, we can conclude that it is also *homogeneous*. The main underlying assumption of cosmology, namely that the Universe is homogeneous and isotropic, is referred to as the *cosmological principle*.

As Hubble (1929) discovered, we live in an expanding Universe. We model this by introducing the *cosmic scale factor* $a(t)$, which describes the relative size of the Universe at cosmic time t with $a(0) = 0$ and $a(t_0) = 1$, where t_0 corresponds to today¹. To describe space in a homogeneous, expanding Universe we introduce *comoving coordinates* \mathbf{x} via $\mathbf{r}(t) = a(t)\mathbf{x}$, where $\mathbf{r}(t)$ is the physical distance between two objects. Assuming zero peculiar velocities, two objects in an expanding Universe always have the same comoving separation.

A light-ray propagating through space is subject to the same expansion, which increases its wavelength in the time between emission and observation by

$$\frac{\lambda_{\text{obs}}}{\lambda_{\text{em}}} = \frac{a(t_{\text{obs}})}{a(t_{\text{em}})}. \quad (2.1)$$

We thus define the *cosmological redshift* z of a comoving source as the ratio between observed and emitted wavelength, $1 + z = \lambda_{\text{obs}}/\lambda_{\text{em}} = 1/a(t_{\text{em}})$.

For the description of a homogeneous and isotropic Universe we use the *Robertson-Walker* metric:

$$ds^2 = c^2 dt^2 - a^2(t) \left[d\chi^2 + f_K^2(\chi) (d\theta^2 + \sin^2\theta d\phi^2) \right]. \quad (2.2)$$

¹ Here, and throughout the rest of this Chapter, we want to denote the value that quantities evolving with time take today, by a subscript 0.

Here, we define t as cosmic time, χ as the comoving radial coordinate and θ and ϕ as the usual angular coordinates. With $f_K(\chi)$ we have denoted the *comoving angular diameter distance*, defined as the unique continuous function satisfying

$$f_K(\chi) = K^{-1/2} \sin(K^{1/2}\chi), \quad (2.3)$$

for all curvature parameters² K . In particular, for $K = 0$, $f_K(\chi) \equiv \chi$ holds. Solving the field equations of general relativity for a homogeneous Universe yields the so-called *Friedmann equations*, which describe the expansion of the Universe over time:

$$\left(\frac{\dot{a}}{a}\right)^2 = \frac{8\pi G}{3}\rho - \frac{Kc^2}{a^2} + \frac{\Lambda}{3}, \quad (2.4)$$

$$\frac{\ddot{a}}{a} = -\frac{4}{3}\pi G\left(\rho + \frac{3p}{c^2}\right) + \frac{\Lambda}{3}. \quad (2.5)$$

The term Λ was introduced by Einstein as a cosmological constant, allowing for a static model of the Universe. Nowadays we know that we live in an expanding, non-static Universe. However, the data strongly suggest that this expansion is accelerating, a phenomenon called *Dark Energy*. This effect can be modelled by a cosmological constant $\Lambda \neq 0$, or by introducing a *vacuum energy* with constant density and negative pressure. We choose the latter way to model Dark Energy and set $\Lambda = 0$.

This means that in the above equations, ρ and p represent the density and pressure of the components constituting the energy budget of the Universe. Note that the equations are linear in both ρ and p , so we can simply take the sum of the contributions by the single components:

- *Matter*, both ordinary and dark. Due to nonrelativistic velocities, $p_m \ll \rho_m c^2$, so the pressure term can be neglected. The density of matter in an expanding spacetime follows $\rho_m(a) \propto a^{-3}$.
- *Radiation*, which consists of photons and relativistic particles such as neutrinos. Here, the pressure can be written as $p_r = \rho_r c^2/3$. As adiabatic decompression is a result of the spacetime expansion, the density term follows $\rho_r(a) \propto a^{-4}$.
- *Dark Energy*, or *Cosmological Constant*, or *Vacuum Energy*. The many names are a hint towards the fact that we have no real idea what Dark Energy actually is. We choose to model it as a fluid with constant density $\rho_\Lambda(a) \equiv \text{const.}$, and negative pressure $p_\Lambda = -\rho_\Lambda c^2$, corresponding to the interpretation of a vacuum energy. Under these assumptions, the equation of state for dark energy is

$$w = \frac{p}{\rho c^2} = -1. \quad (2.6)$$

A popular extension to the standard model of cosmology is the introduction of a time-varying dark energy, whose equation of state is parametrized as

$$w(a) = w_0 + w_a(1 - a), \quad (2.7)$$

corresponding to the first order Taylor polynomial of an arbitrary equation of state.

The total energy density of the Universe can thus be written as

$$\rho_{\text{tot}} = \rho_m + \rho_r + \rho_\Lambda = \frac{\rho_{m0}}{a^3} + \frac{\rho_{r0}}{a^4} + \rho_{\Lambda 0}. \quad (2.8)$$

² The case $K < 0$ is accounted for by complex notation.

If we now define the expansion rate of the Universe as

$$H(t) = \frac{\dot{a}}{a}, \quad (2.9)$$

and $H_0 := H(t_0)$, we can find the critical density today, at which the curvature vanishes ($K = 0$), from Eq. (2.4):

$$\rho_{\text{cr}} = \frac{3H_0^2}{8\pi G}. \quad (2.10)$$

Using this, we can define the *dimensionless density parameters* as

$$\Omega_x = \frac{\rho_{x0}}{\rho_{\text{cr}}} \quad (2.11)$$

for $x \in \{m, r, \Lambda\}$. This allows us to write the expansion equation as

$$H^2(t) = H_0^2 \left[\frac{\Omega_r}{a^4} + \frac{\Omega_m}{a^3} - \frac{Kc^2}{a^2 H_0^2} + \Omega_\Lambda \right]. \quad (2.12)$$

As it turns out, the curvature in our Universe is extremely close to or equal zero, which is why from here on forward we want to assume a *flat Universe* with zero curvature. The expansion equation contains some of the main cosmological parameters:

- The *Hubble constant* H_0 basically describes the current size of the Universe. It is mostly parametrized as

$$H_0 = 100 h \text{ km s}^{-1} \text{ Mpc}^{-1}, \quad (2.13)$$

where h describes our lack of knowledge for the precise value. Nowadays, the value of $h \approx 0.67$ determined by Planck Collaboration et al. (2018) is mostly assumed.

- The *radiation density* $\Omega_r \approx 3.2 \times 10^{-5} h^{-2}$ mostly governs the early evolution of the Universe, at small scale factors a . It is very well-constrained from the temperature of the Cosmic Microwave Background.
- The *matter density* $\Omega_m \approx 0.3$ is the main contributor to the evolution of structure. The scale factor of matter-radiation equality $a_{\text{eq}} = \Omega_r / \Omega_m \approx 10^{-4} h^{-2}$ describes since when matter has been the governing component of the Friedmann equation. It has only recently ($a \approx 0.75$) lost this role to dark energy.
- The *vacuum energy density* $\Omega_\Lambda \approx 0.7$ became the main component of the Friedmann equation and is responsible for the accelerated expansion of the Universe. For redshifts $z \gtrsim 2$ however it is negligible.

The precise determination of those cosmological parameters is one of the main challenges in modern cosmology.

2.1.2 Distances in cosmology

As the spacetime described by the Robertson-Walker metric is not Minkowski, there is no unambiguous way to define the distance to an object, as we do not measure Euclidean distance, but rather a distance along a light-cone propagating through an expanding Universe. However, there are some ways to define distances, and we will give a brief overview:

- The *Comoving Distance* χ of an object at redshift z can be calculated via

$$\chi(z) = \int_0^z dz \frac{c}{H(z)}. \quad (2.14)$$

- The *Angular Diameter Distance* D_{ang} is (under the usually valid small-angle-approximation) defined as the ratio of an object's physical diameter D divided by its angular diameter δ :

$$D_{\text{ang}}(z) = \frac{D}{\delta} = \frac{\chi(z)}{1+z}. \quad (2.15)$$

More generally, an observer at redshift z_1 sees an object at z_2 at angular diameter distance

$$D_{\text{ang}}(z_1, z_2) = a(z_2) [\chi(z_2) - \chi(z_1)]. \quad (2.16)$$

Note that, in particular, $D_{\text{ang}}(z_1, z_2) \neq D_{\text{ang}}(z_2) - D_{\text{ang}}(z_1)$ holds. It is interesting to observe that the angular diameter distance is not a monotonic function of redshift: Due to the fact that the Universe was much smaller at e.g. $z = 2$, the same object at that redshift actually appears *larger* than it would at $z = 1.7$, although being further away.

- The *Luminosity Distance* D_{lum} relates the luminosity L of an object to the observed flux S . In analogy to the Euclidean version, we define

$$D_{\text{lum}}(z) \equiv \sqrt{\frac{L}{4\pi S}} = (1+z)\chi(z). \quad (2.17)$$

- The *Light-travel Distance* D_γ measures the light travel time τ from an object to the observer, multiplied by the speed of light c . We define

$$D_\gamma(z) \equiv c\tau = \int_0^z dz \frac{c}{(1+z)H(z)}. \quad (2.18)$$

Due to the finite age of the Universe and the fact that information can not travel faster than light, at any scale factor a there is a maximum size for regions that have been in causal contact since the beginning of the Universe, called the *comoving horizon size* d_{H} , which equates to approximately

$$d_{\text{H}} \approx \frac{c}{aH(a)}. \quad (2.19)$$

2.1.3 Structure growth

As a local observer the sentence "The Universe is homogeneous" seems a bit bizarre, standing on the earth, looking up and seeing isolated stars and galaxies, all of which certainly prove that the Universe can not be completely homogeneous. Indeed, homogeneity only applies when one observes scales larger than $\sim 200 h^{-1}$ Mpc. Still, the question, how those inhomogeneities formed, and what their origin is, remains.

Following the standard model of cosmology, we believe that for an extremely brief period after the big bang, random quantum fluctuations got blown up to macroscopic scales during the so-called *inflation*. Those tiny inhomogeneities are the seeds of the structure that we observe today. To model their evolution,

we define the *density contrast* $\delta(\mathbf{x}, t)$ as

$$\delta(\mathbf{x}, t) = \frac{\rho(\mathbf{x}, t) - \bar{\rho}(t)}{\bar{\rho}(t)}, \quad (2.20)$$

where $\bar{\rho}(t)$ denotes the average matter density at cosmic time t . For the first few hundred thousand years, these inhomogeneities were extremely small: During the time when the CMB radiation last interacted with matter, at $z \sim 1100$, the density contrast was of the order of $\delta \sim 10^{-5}$. This implies, that we can perform a linearized treatment of this problem to achieve an analytical solution. Once the density contrast rises to an order of unity, one has to rely on heavy numerical calculations or simulations.

For a first analysis, we want to assume that matter constitutes the only component of the Friedmann equation (2.12). This assumption is valid for a broad range of cosmic scale factors, especially in the linear part of structure formation. Additionally, we assume that the density perturbations are small in size (meaning that they are much smaller than the comoving horizon size d_H at that time), which allows us to work with Newtonian gravity instead of general relativity. Under these assumptions, the linearized continuity, Euler and Poisson equations yield a second order, homogeneous linear differential equation describing the evolution of the density contrast (compare e.g. Schneider 2015):

$$\ddot{\delta} + \frac{2\dot{a}}{a}\dot{\delta} - \frac{3H_0^2\Omega_m}{2a^3}\delta = 0. \quad (2.21)$$

This equation allows for two linearly independent solutions

$$\delta(\mathbf{x}, t) = D_+(t)\Delta_+(\mathbf{x}) + D_-(t)\Delta_-(\mathbf{x}), \quad (2.22)$$

where the solution D_- is decaying with time and therefore not important for the evolution of structure. We find

$$\delta(\mathbf{x}, t) = D_+(t)\delta_0(\mathbf{x}), \quad (2.23)$$

where $\delta_0(\mathbf{x}) = \delta(\mathbf{x}, t_0)$ is the *linearly extrapolated density contrast* and

$$D_+(t) \propto H(t) \int_0^{a(t)} \frac{da'}{[a'H(a')]^3}, \quad (2.24)$$

such that $D_+(t_0) = 1$ holds. In the Λ CDM-model, $D_+(t) > a(t)$ holds at all cosmic times $t < t_0$.

While this approach yields a nice and simple solution, and can be used for a large part of structure growth, we can not use it to describe the evolution from the initial density contrasts originating during inflation to the structure we observe today.

For $a < a_{\text{eq}}$, radiation dominated the energy budget of the Universe, implying a different behaviour of the expansion governed by Eq. (2.12). Assuming $a \ll a_{\text{eq}}$ yields $\delta = \text{const.}$ for the radiation dominated phase.

During inflation, the density perturbations were blown up to macroscopic scales. After that phase, those perturbations were larger than the horizon size d_H , which means that we have to treat their evolution using general relativity. After some time, the perturbations *entered the horizon*, meaning d_H got large enough to encompass them, and we can treat them with the Newtonian equations again.

To mitigate these effects, the *transfer function* T_k is introduced. When $\tilde{\delta}(\mathbf{k}, t)$ describes the Fourier transform of $\delta(\mathbf{x}, t)$, then the transfer function T_k describes the ratio of the real density contrast $\tilde{\delta}(\mathbf{k}, t)$ and the idealized one, which neglects the effects of superhorizon perturbations and radiation-dominated

expansion, $\tilde{\delta}_{\text{ideal}}(\mathbf{k}, t)$:

$$T_k = \frac{\tilde{\delta}(\mathbf{k}, t)}{\tilde{\delta}_{\text{ideal}}(\mathbf{k}, t)}. \quad (2.25)$$

This allows us to predict the evolution of cosmic structure until the point where a nonlinear treatment is necessary. In order to predict the non-linear regime of the power spectrum, several methods have been developed to emulate results from numerical simulations (compare e.g. Takahashi et al. 2012; Heitmann et al. 2014). Even if we can perfectly predict the evolution of a density contrast, we will never be able to reproduce the one of our Universe. We can, however, compare statistical properties of our models with measured ones. For this we introduce the *correlation function*

$$C_\delta(|\mathbf{x} - \mathbf{y}|) \equiv \langle \delta(\mathbf{x}) \delta^*(\mathbf{y}) \rangle. \quad (2.26)$$

Due to the fact that the Universe is homogeneous and isotropic, the value of the correlation function only depends on the modulus of the separation vector. Under these assumptions, we can calculate the Fourier transform of the correlation function, the *power spectrum*, via

$$(2\pi)^3 \delta_D(\mathbf{k} - \mathbf{k}') P_\delta(|\mathbf{k}|) = \langle \tilde{\delta}(\mathbf{k}) \tilde{\delta}^*(\mathbf{k}') \rangle, \quad (2.27)$$

where δ_D denotes the Dirac delta functional. We can calculate the time-evolution of the power spectrum in the matter dominated cosmic times via

$$P_\delta(k, t) = D_+^2(t) P_0(k), \quad (2.28)$$

where $P_0(k)$ is the *linearly extrapolated* power spectrum at $t = t_0$. Said power spectrum is mostly assumed to be a power law k^{n_s} with the *spectral index* n_s constrained by most inflation models to $n_s \lesssim 1$, which is backed by observations (compare e.g. Planck Collaboration et al. 2018). Applying the transfer function, this yields

$$P_0(|\mathbf{k}|) = A k^{n_s} T_k^2. \quad (2.29)$$

The only free parameter left is the normalisation of the power spectrum. The usual method to fix this normalisation is called σ_8 , which is the Amplitude of the linear power spectrum at scales of $8 h^{-1} \text{ Mpc}$. More formally, we can set (compare Rich 2001)

$$\sigma_R^2 = \int_0^\infty \frac{dk}{k} \frac{k^3 P(k)}{2\pi^2} W^2(kR) \quad \text{with} \quad W(x) = 3 \left[\frac{\sin(x)}{x^3} - \frac{\cos(x)}{x^2} \right]. \quad (2.30)$$

This parameter can be determined by various methods, for example by comparing the observed abundance of clusters with the expected one. Using this, Eke, Cole and Frenk (1996) determined a value of $\sigma_8 = 0.52 \Omega_m^{-0.52+0.13\Omega_m}$. As cosmic shear surveys show a similar degeneracy between σ_8 and Ω_m , we introduce the parameter

$$S_8 = \sigma_8 \sqrt{\Omega_m/0.3}, \quad (2.31)$$

which can be determined with a much greater accuracy.

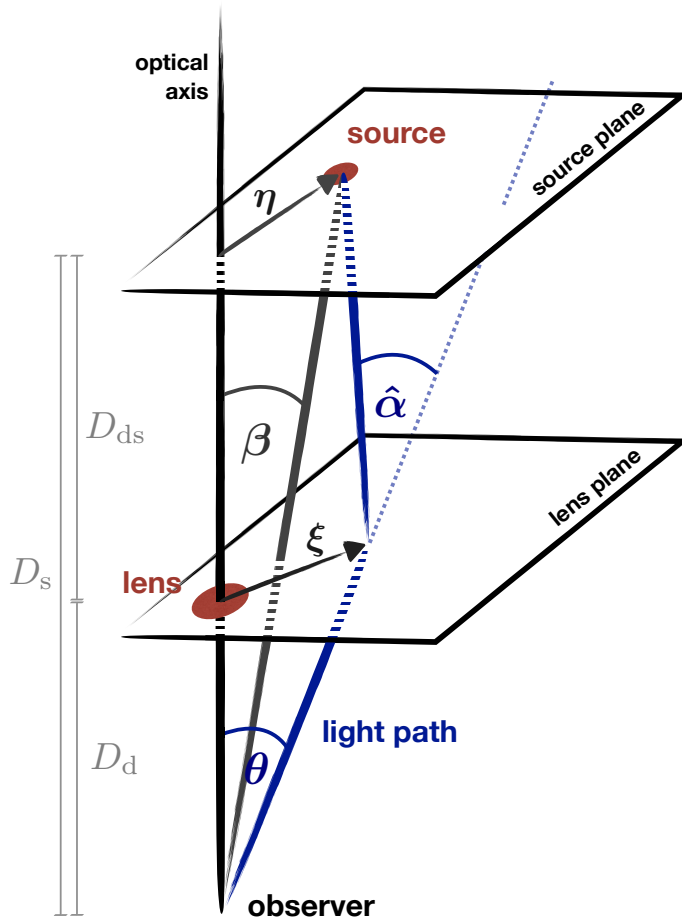


Figure 2.1 – Sketch of a gravitational lensing event. Adapted from Bartelmann and Schneider (2001), created by S. Unruh.

2.2 Gravitational lensing

In this section we will describe the theoretical framework of gravitational lensing, which is necessary to understand the following parts of this thesis. We will especially focus on weak gravitational lensing and cosmic shear, as those are the important aspects for the following chapters.

2.2.1 Theoretical framework

One of the main predictions of general relativity is that photons follow geodesic curves in spacetime and are thus affected by the local curvature, which is caused by the presence of mass. Whenever the (Newtonian) gravitational potential Φ is small, meaning $\Phi/c^2 \ll 1$, we can linearize the field equations of general relativity, which allows for a simplified treatment. In particular we can simply treat the contributions of different masses individually. As the gravitational potential in the entire Universe, except for the vicinity of black holes and neutron stars, is small, we can apply such a linearized treatment: If a light ray passes a mass M at an impact angle of ξ , general relativity predicts a deflection angle of

$$\hat{\alpha} = \frac{4GM}{c^2 \xi}. \quad (2.32)$$

If we assume photons to have an (infinitesimal) mass, we can also calculate a deflection angle under Newtonian gravity, which coincidentally is exactly half as large. Measurements of this deflection angle during a solar eclipse by Dyson, Eddington and Davidson (1920) served as one of the first tests of General Relativity.

In general, when we treat a gravitational lensing event, we define D_d as the (angular diameter) distance³ to the deflector, D_s as the distance to the source and D_{ds} as the distance between deflector and source, we can imagine a gravitational lensing event like in Figure 2.1. Here, we assume that the extent of both lens and source are small in comparison to the involved distances, which is usually known as the *thin lens approximation*. Also, we work in the small-angle approximation, meaning that $\sin(\alpha) = \tan(\alpha) = \alpha$ for all relevant angles α . As angles in lensing are usually of the order of a few arcseconds, this assumption will not cause us any trouble whatsoever. Simple geometry in Figure 2.1 dictates

$$\boldsymbol{\eta} = \frac{D_s}{D_d} \boldsymbol{\xi} - D_{ds} \hat{\boldsymbol{\alpha}}(\boldsymbol{\xi}). \quad (2.33)$$

This we can transform to

$$\boldsymbol{\beta} = \boldsymbol{\theta} - \frac{D_{ds}}{D_s} \hat{\boldsymbol{\alpha}}(D_d \boldsymbol{\theta}) \equiv \boldsymbol{\theta} - \boldsymbol{\alpha}(\boldsymbol{\theta}), \quad (2.34)$$

by introducing the *scaled deflection angle*

$$\boldsymbol{\alpha}(\boldsymbol{\theta}) = \frac{D_{ds}}{D_s} \hat{\boldsymbol{\alpha}}(D_d \boldsymbol{\theta}). \quad (2.35)$$

As previously stated, we can linearize the field equations, so we can calculate the total deflection caused by a mass as a sum or, in the more realistic case of a continuous mass distribution, as an integral of the single contributions. Introducing the surface mass density

$$\Sigma(\boldsymbol{\xi}) \equiv \int d r_3 \rho(\xi_1, \xi_2, r_3), \quad (2.36)$$

as an integral over the three-dimensional density ρ , we can calculate the deflection angle as

$$\hat{\boldsymbol{\alpha}}(\boldsymbol{\xi}) = \frac{4G}{c^2} \int d^2 \xi' \Sigma(\boldsymbol{\xi}') \frac{\boldsymbol{\xi} - \boldsymbol{\xi}'}{|\boldsymbol{\xi} - \boldsymbol{\xi}'|^2}. \quad (2.37)$$

Introducing the *critical surface mass density* Σ_{cr} and the *convergence* κ via

$$\Sigma_{cr} = \frac{c^2}{4\pi G} \frac{D_s}{D_d D_{ds}} \quad \text{and} \quad \kappa(\boldsymbol{\theta}) = \frac{\Sigma(D_d \boldsymbol{\theta})}{\Sigma_{cr}}, \quad (2.38)$$

the scaled deflection angle $\boldsymbol{\alpha}$ can be written as

$$\boldsymbol{\alpha}(\boldsymbol{\theta}) = \frac{1}{\pi} \int d^2 \theta' \kappa(\boldsymbol{\theta}') \frac{\boldsymbol{\theta} - \boldsymbol{\theta}'}{|\boldsymbol{\theta} - \boldsymbol{\theta}'|}. \quad (2.39)$$

We define the deflection potential Ψ via

$$\Psi(\boldsymbol{\theta}) = \frac{1}{\pi} \int d^2 \theta' \kappa(\boldsymbol{\theta}') \ln |\boldsymbol{\theta} - \boldsymbol{\theta}'|, \quad (2.40)$$

³ Whenever we speak of distance in gravitational lensing, unless otherwise specified, it will be the angular diameter distance.

and obtain the identities

$$\alpha(\boldsymbol{\theta}) = \nabla \Psi(\boldsymbol{\theta}) \quad \text{and} \quad \nabla^2 \Psi(\boldsymbol{\theta}) = 2\kappa(\boldsymbol{\theta}). \quad (2.41)$$

The Jacobian of the lens equation then reads

$$\mathcal{A}(\boldsymbol{\theta}) = \frac{\partial \boldsymbol{\beta}}{\partial \boldsymbol{\theta}}(\boldsymbol{\theta}) = \left(\delta_{ij} - \frac{\partial^2 \Psi(\boldsymbol{\theta})}{\partial \theta_i \partial \theta_j} \right) = \begin{pmatrix} 1 - \kappa - \gamma_1 & -\gamma_2 \\ -\gamma_2 & 1 - \kappa + \gamma_1 \end{pmatrix}, \quad (2.42)$$

where we have introduced the *shear* $\gamma = \gamma_1 + i\gamma_2 = |\gamma|e^{2i\varphi}$, and

$$\gamma_1 = \frac{1}{2}(\Psi_{,11} - \Psi_{,22}) \quad \text{and} \quad \gamma_2 = \Psi_{,12}. \quad (2.43)$$

If $\det(\mathcal{A}) \neq 0$ over the whole parameter space, then the lens mapping is invertible and we have a direct correspondence between image and source. However, when the determinant $\det(\mathcal{A})$ becomes zero, the mapping $\boldsymbol{\beta} \rightarrow \boldsymbol{\theta}$ is no longer invertible. These points are called *critical curves*, and on those the magnification⁴

$$\mu \equiv \left| \frac{d^2 \boldsymbol{\beta}}{d^2 \boldsymbol{\theta}} \right|^{-1} = |\det(\mathcal{A})|^{-1} \quad (2.44)$$

diverges. Wherever the convergence is big enough that the magnification can diverge, we speak of *strong gravitational lensing*. A variety of interesting phenomena can be observed in these regimes: Strong distortions and magnifications as well as the creation of multiple images are only the figurative tip of the iceberg. However, this thesis will work in the regime of *weak gravitational lensing*, where the gravitational light deflection is not strong enough for that to happen. An interested reader can find more information about strong lensing in Schneider (2015).

2.2.2 Weak lensing and cosmic shear

In weak gravitational lensing we focus on the shape distortions of galaxies caused by the tidal gravitational field of a deflector. Reviewing Eq. (2.42), we see that the term $(1 - \kappa)$ is responsible for a uniform increase or decrease in image size, which we can not measure, as the intrinsic size of a galaxy is unknown. We can, however, write our distortion matrix as

$$\mathcal{A}(\boldsymbol{\theta}) = (1 - \kappa) \begin{pmatrix} 1 - g_1 & -g_2 \\ -g_2 & 1 + g_1 \end{pmatrix}, \quad (2.45)$$

with the *reduced shear*

$$g(\boldsymbol{\theta}) = \frac{\gamma(\boldsymbol{\theta})}{1 - \kappa(\boldsymbol{\theta})}. \quad (2.46)$$

If we now measure the ellipticity ϵ of a galaxy, it is dominated by its unknown intrinsic shape and the gravitational shear only plays a subdominant role. However, as the intrinsic ellipticities of galaxies are random according to the cosmological principle, the expectation value $\langle \epsilon \rangle$ still equals the reduced shear g , which makes it an unbiased estimator for the local shear (C. Seitz and Schneider 1997; Schramm and Kayser 1995).

Assuming we can measure a shear field $\gamma(\boldsymbol{\theta})$, we can reconstruct the convergence field $\kappa(\boldsymbol{\theta})$: Following

⁴ As the number of photons does not change due to a gravitational lensing event, surface brightness is always conserved. This means that the magnification is simply the ratio of lensed to unlensed solid angle.

Kaiser and Squires (1993), given the function

$$\mathcal{D}(\boldsymbol{\theta}) = \frac{\theta_2^2 - \theta_1^2 - 2i\theta_1\theta_2}{|\boldsymbol{\theta}|^4}, \quad (2.47)$$

a given convergence κ leads to a shear field γ by convolution with the kernel \mathcal{D} :

$$\gamma(\boldsymbol{\theta}) = \frac{1}{\pi} \int d^2\theta' \mathcal{D}(\boldsymbol{\theta} - \boldsymbol{\theta}') \kappa(\boldsymbol{\theta}') \equiv \frac{1}{\pi} [\mathcal{D} * \kappa](\boldsymbol{\theta}). \quad (2.48)$$

Conversely, given a shear field γ we obtain a convergence field κ (up to a uniform mass sheet κ_0 , which causes no shear) via

$$\kappa(\boldsymbol{\theta}) - \kappa_0 = \frac{1}{\pi} [\mathcal{D}^* * \gamma](\boldsymbol{\theta}). \quad (2.49)$$

Observationally, this obviously induces several challenges: First, we can not observe the shear field for every position $\boldsymbol{\theta}$, rather we can only measure it at certain positions, where we find galaxies. This can usually be mitigated by smoothing the observed shears of the galaxies with a given kernel. Additionally, the convolutions with the kernel \mathcal{D} assume an infinite field, which is also not realistic. More sophisticated methods have been developed for finite field mass reconstructions (see e.g. S. Seitz and Schneider 2001), but for our scope this shall suffice. One might notice that the convergence field κ is supposed to be a real function, whereas both \mathcal{D}^* and γ are complex functions. Indeed, for a shear field caused by an arbitrary convergence field, the convolution yields a real field. In realistic cases, where noise and systematics are involved, κ will not be a real function. We will treat these cases in Section 2.2.3.

As the Universe is homogeneous and isotropic, the correlation function

$$C_{\gamma\gamma}(|\boldsymbol{\theta} - \boldsymbol{\theta}'|) \equiv \langle \gamma(\boldsymbol{\theta}) \gamma^*(\boldsymbol{\theta}') \rangle, \quad (2.50)$$

depends only on the separation $|\boldsymbol{\theta} - \boldsymbol{\theta}'|$, and we can define the power spectrum $P_\gamma(|\boldsymbol{\ell}|)$ via

$$\langle \tilde{\gamma}(\boldsymbol{\ell}) \tilde{\gamma}(\boldsymbol{\ell}') \rangle \equiv (2\pi)^2 \delta_D(\boldsymbol{\ell} - \boldsymbol{\ell}') P_\gamma(|\boldsymbol{\ell}|). \quad (2.51)$$

Applying the convolution theorem to (2.49) and seeing that $\tilde{\mathcal{D}}(\boldsymbol{\ell}) \tilde{\mathcal{D}}^*(\boldsymbol{\ell}) = \pi^2$ for $\boldsymbol{\ell} \neq \mathbf{0}$, one finds $P_\kappa(\boldsymbol{\ell}) = P_\gamma(\boldsymbol{\ell})$. It is important to note that the convergence power spectrum is not well-defined for $\boldsymbol{\ell} = \mathbf{0}$, which makes perfect sense, as the mode $\boldsymbol{\ell} = \mathbf{0}$ corresponds to a uniform mass sheet, which can not be detected from shear (compare Eq. 2.49).

Although the shear γ has two components and thus looks like a vector, it behaves differently under rotations: While a vector changes sign under rotation by 180° , the shear is invariant under this transformation. However, we can define a sometimes more convenient coordinate system to measure shear. If we fix an arbitrary point p on the sky and define ϕ as the angle between p and the point where we measure the shear, then we can define *tangential* and *cross components* of the shear as (compare Figure 2.2)

$$\gamma_t = -\Re[\gamma e^{-2i\phi}] \text{ and } \gamma_\times = -\Im[\gamma e^{-2i\phi}]. \quad (2.52)$$

In general, if our point p is an overdensity, we will measure positive tangential shear, if it is an underdensity one measures negative tangential shear. In particular, the expectation value of tangential shear at an arbitrary radius r around our chosen point reads

$$\langle \gamma_t \rangle = \bar{\kappa} - \langle \kappa \rangle, \quad (2.53)$$

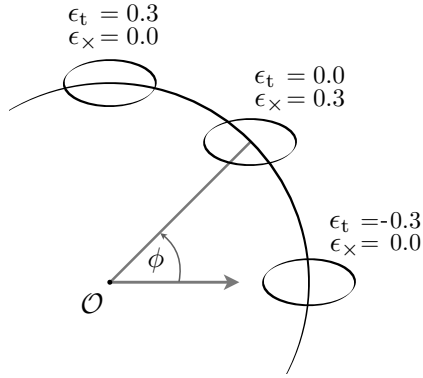


Figure 2.2 – Tangential and cross components of the shear for a galaxy under different inclination angles ϕ . This figure was adapted from work by M. Bradac in Schneider (2012) and created by S. Unruh.

where $\bar{\kappa}$ is the mean convergence *within* radius r , whereas $\langle \kappa \rangle$ denotes the mean convergence at r .

The underlying idea of cosmic shear bases on the principles of weak gravitational lensing. The light from a distant galaxy, passing through the 3D matter distribution on its way to the observer, is sheared in the same way as in weak lensing. However, contrary to the weak lensing case, the thin-lens approximation is no longer valid – matter is distributed along the entire light-path. Considering this, it is impossible to make any predictions based off the shearing of single galaxies. However, if a second galaxy lies close to the first one, its light passes a similar gravitational field and its image will thus be similarly sheared. When we measure the correlation of those shears, in dependence of the distance between the galaxies, we can estimate how much matter is located between the galaxies and the observer, and how strongly clustered it is. As the thin-lens approximation is no longer valid, we have to develop a new formalism to describe light propagation through matter inhomogeneities. We will not be able to go into too much detail, the interested reader can find more information in Bartelmann and Schneider (2001).

Assume a galaxy at comoving distance χ emits a bundle of light that gets detected by an observer on Earth. This bundle travelled along a geodesic path through the 3D matter distribution of the Universe and got deflected and distorted along the way. It can be shown (compare e.g. Bartelmann and Schneider 2001), that we can still apply our standard lensing formalism by replacing the convergence κ with the effective surface mass density

$$\kappa_{\text{eff}}(\boldsymbol{\theta}, \chi) = \frac{3H_0^2 \Omega_m}{2c^2} \int_0^\chi d\chi' \frac{\chi'(\chi - \chi')}{\chi} \frac{\delta(\chi' \boldsymbol{\theta}, \chi')}{a(\chi')}. \quad (2.54)$$

However, as we will not limit our analysis to a single galaxy, but instead perform it on a sample with comoving distance distribution $p(\chi)$, we need to consider the convergence

$$\begin{aligned} \kappa(\boldsymbol{\theta}) &= \int d\chi p(\chi) \kappa_{\text{eff}}(\boldsymbol{\theta}, \chi) \\ &= \frac{3H_0^2 \Omega_m}{2c^2} \int d\chi g(\chi) \chi \frac{\delta(\chi \boldsymbol{\theta}, \chi)}{a(\chi)} \end{aligned} \quad (2.55)$$

with the *lens efficiency*

$$g(\chi) = \int_\chi^\infty d\chi' p(\chi') \frac{\chi' - \chi}{\chi'}. \quad (2.56)$$

While this result is certainly handy, we would still need to determine the actual density contrast field δ , which is impossible. We can, however, determine its statistical measures, like the density power spectrum P_δ . Following Kaiser (1992), we see that the convergence power spectrum P_κ^{ij} of two galaxy samples i

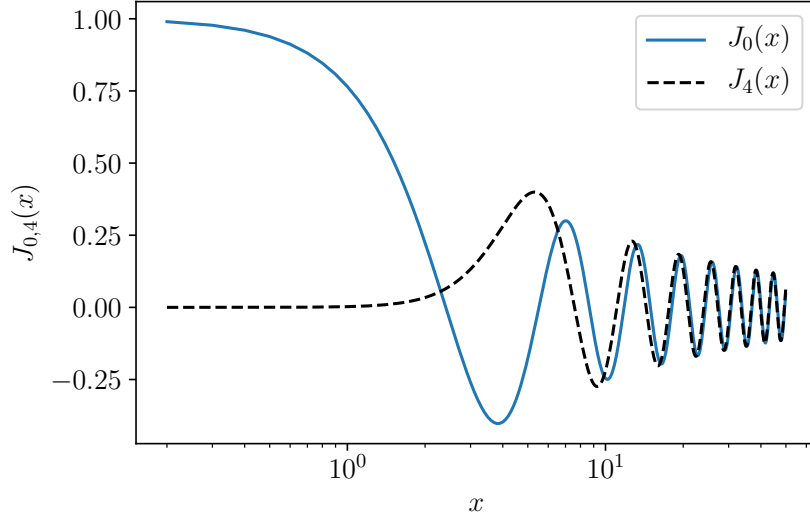


Figure 2.3 – 0-th and 4-th order Bessel Functions of first kind.

and j with comoving distance distributions $p_i(\chi)$ and $p_j(\chi)$ can be written as

$$P_{\kappa}^{ij}(\ell) = \frac{9H_0^4\Omega_m^2}{4c^4} \int d\chi \frac{g_i(\chi)g_j(\chi)}{a^2(\chi)} P_{\delta} \left[\frac{\ell}{\chi}, \chi \right], \quad (2.57)$$

with $g_i(\chi)$ and $g_j(\chi)$ as in Eq. (2.56) and P_{δ} as in (2.28). This equation relates an observable P_{κ} to a cosmological model via P_{δ} , which in theory allows us to constrain the parameters of the standard model. Practically, however, it is relatively difficult to determine the power spectrum from observations. Finite field effects, masked areas and different weighting of galaxies all make the determination of the shear power spectrum, from which we can determine the convergence power spectrum, extremely difficult (albeit not impossible). We thus would prefer to use a shear statistic that is more straightforward to determine from observations:

When we consider a pair of galaxies with ellipticities ϵ^i and ϵ^j and distance θ , we can use Eq. (2.52) to define their tangential and cross shear *with respect to each other*. We can then define the correlations of tangential and cross shear via

$$\langle \gamma_t \gamma_t \rangle(\theta) \equiv \langle \epsilon_t^i \epsilon_t^j \rangle, \quad \langle \gamma_{\times} \gamma_{\times} \rangle(\theta) \equiv \langle \epsilon_{\times}^i \epsilon_{\times}^j \rangle \quad \text{and} \quad \langle \gamma_t \gamma_{\times} \rangle(\theta) \equiv \langle \epsilon_t^i \epsilon_{\times}^j \rangle. \quad (2.58)$$

Following Kaiser (1992), one finds

$$\left(\frac{\langle \gamma_t \gamma_t \rangle(\theta)}{\langle \gamma_{\times} \gamma_{\times} \rangle(\theta)} \right) = \frac{1}{2} \int \frac{d\ell}{2\pi} P_{\kappa}(\ell) \left(\frac{J_0(\ell\theta) + J_4(\ell\theta)}{J_0(\ell\theta) - J_4(\ell\theta)} \right), \quad (2.59)$$

and $\langle \gamma_t \gamma_{\times} \rangle = 0$ due to parity symmetry. Here, J_n denotes the n -th order Bessel Function of first kind, as can be seen in Figure 2.3. If we now define the shear correlation functions as

$$\xi_{\pm}(\theta) \equiv \langle \gamma_t \gamma_t \rangle \pm \langle \gamma_{\times} \gamma_{\times} \rangle, \quad (2.60)$$

given two galaxy samples i and j they can be calculated from the convergence power spectrum via

$$\xi_{\pm}^{ij}(\theta) = \int \frac{d\ell}{2\pi} \ell J_{0,4}(\ell\theta) P_{\kappa}^{ij}(\ell). \quad (2.61)$$

As a first check for systematics one can calculate the function $\xi_{\times}(\theta)$ defined via

$$\xi_{\times}(\theta) \equiv \langle \gamma_t \gamma_{\times} \rangle, \quad (2.62)$$

which should be consistent with zero. Observationally, given two galaxy samples i and j with lensing-weights w_a^i, w_b^j and ellipticities $\epsilon_a^i, \epsilon_b^j$, we can calculate the correlation functions via (compare Hildebrandt et al. 2017)

$$\xi_{\pm}^{ij}(\theta) = \frac{\sum_{a,b} w_a^i w_b^j [\epsilon_{t,b}^i \epsilon_{t,b}^j \pm \epsilon_{\times,a}^i \epsilon_{\times,b}^j] \Delta(|\theta_b^j - \theta_a^i|)}{\sum_{a,b} w_a^i w_b^j \Delta(|\theta_b^j - \theta_a^i|)}, \quad (2.63)$$

where $\Delta(|\theta_b^j - \theta_a^i|)$ equals 1 when the respective galaxies have separation θ , and 0 otherwise.

We now have a shear statistic that is relatively easy⁵ to determine from observational data, and we are able to obtain it from a cosmological model. We can thus simply compare the correlation functions we measure with our model ones to see which values for the cosmological parameters are favoured.

2.2.3 Separating E- and B-modes in gravitational lensing

The field of weak gravitational lensing poses a significant number of observational and statistical challenges. We want to measure a tiny distortion in shapes of galaxies, whose size often is smaller than the point-spread function of our telescope. Many systematic effects, like intrinsic alignment of galaxies or a position-dependent ellipticity of the point-spread function are extremely difficult to disentangle from the real lensing signal. For that reason it is crucial to have a reliable check for remaining systematic effects in one's survey.

There are several ways to split a lensing signal into so-called E- and B-modes. These are constructed in a way that B-modes can, to leading order, not be created by gravitational lensing. This means that any B-modes in a survey are a sign of remaining systematic effects that have not been accounted for. It is important to keep in mind that a B-mode free sample is not necessarily free of systematics. In this section we will introduce a few methods to determine B-modes in gravitational lensing.

As previously mentioned, the mass reconstruction following Eq. (2.49) yields a complex convergence field. If we define our E- and B-modes of a measured shear field γ as

$$\kappa^E = \frac{1}{\pi} \Re [\mathcal{D}^* * \gamma] \text{ and } \kappa^B = \frac{1}{\pi} \Im [\mathcal{D}^* * \gamma], \quad (2.64)$$

we have achieved our first E- and B-mode decomposition. While this is not a feasible method for a decomposition of observed data, it does help us to construct other ways to split a real signal. Following

⁵ A lot of complications arise when determining the shear correlation function. From the determination of the comoving distance distribution of our galaxies, the effect of intrinsic alignments, galaxy-galaxy lensing and baryonic feedback to observational effects, many aspects need to be considered. However, there is no other shear statistic that allows one to circumvent one of those problems, which makes the shear correlation functions the most conveniently used statistics when working with cosmic shear.

Schneider, van Waerbeke and Mellier (2002), we define E- and B-mode power spectra via

$$\begin{aligned}\langle \tilde{\kappa}^E(\ell) \tilde{\kappa}^{E*}(\ell') \rangle &= (2\pi)^2 \delta_D(\ell - \ell') P_E(\ell), \\ \langle \tilde{\kappa}^B(\ell) \tilde{\kappa}^{B*}(\ell') \rangle &= (2\pi)^2 \delta_D(\ell - \ell') P_B(\ell), \\ \langle \tilde{\kappa}^E(\ell) \tilde{\kappa}^{B*}(\ell') \rangle &= (2\pi)^2 \delta_D(\ell - \ell') P_{EB}(\ell).\end{aligned}\quad (2.65)$$

One can determine those from the shear correlation functions following

$$\begin{aligned}P_E(\ell) &= \pi \int_0^\infty d\theta \theta [\xi_+(\theta) J_0(\ell\theta) + \xi_-(\theta) J_4(\ell\theta)], \\ P_B(\ell) &= \pi \int_0^\infty d\theta \theta [\xi_+(\theta) J_0(\ell\theta) - \xi_-(\theta) J_4(\ell\theta)], \\ P_{EB}(\ell) &= 2\pi \int_0^\infty d\theta \theta \xi_\times(\theta) J_4(\ell\theta).\end{aligned}\quad (2.66)$$

The problem with this method is that the integral over the shear correlation functions spans from zero to infinity. We can not determine the correlation functions to arbitrarily small angles due to finite sizes of galaxies⁶, and due to a finite survey footprint the determination up to arbitrarily large angles is also impossible (apart from the fact that at some angles the flat-sky approximation would not be valid anymore). Many other methods, like the splitting into E- and B- mode correlation functions $\xi_{\pm,E}$ and $\xi_{\pm,B}$ (compare Schneider, van Waerbeke and Mellier 2002) suffer from the same problem. We would thus like a method to split shear correlation functions from a minimal angle θ_{\min} to a (finite) maximum angle θ_{\max} into E- and B-modes. For this we use the Complete Orthogonal Sets of E- and B-mode Integrals (COSEBIs) developed by Schneider, Eifler and Krause (2010). They allow a separation of modes using finite integrals over the shear correlation functions:

Schneider and Kilbinger (2007) showed that an E- and B-mode separation can be achieved by filter functions T_\pm via

$$\begin{aligned}E &= \frac{1}{2} \int_0^\infty d\theta \theta [T_+(\theta) \xi_+(\theta) + T_-(\theta) \xi_-(\theta)], \\ B &= \frac{1}{2} \int_0^\infty d\theta \theta [T_+(\theta) \xi_+(\theta) - T_-(\theta) \xi_-(\theta)],\end{aligned}\quad (2.67)$$

as long as these functions obey

$$\int_0^\infty d\theta \theta T_+(\theta) J_0(\ell\theta) = \int_0^\infty d\theta \theta T_-(\theta) J_4(\ell\theta). \quad (2.68)$$

While the integral itself still spans the interval $[0, \infty]$, we can choose filter functions T_+ with finite support $[\theta_{\min}, \theta_{\max}]$ that obey

$$\int_{\theta_{\min}}^{\theta_{\max}} d\theta \theta T_+(\theta) = 0 = \int_{\theta_{\min}}^{\theta_{\max}} d\theta \theta^3 T_+(\theta), \quad (2.69)$$

then this condition ensures that $T_-(\theta)$ has the same (finite) support and the Integral (2.67) to determine the E- and B-modes has a finite support as well (compare Schneider and Kilbinger 2007). Schneider, Eifler and Krause (2010) developed a complete set of filter functions $T_{n\pm}$ that obey the above mentioned

⁶ Also, intrinsic alignments and galaxy-galaxy lensing would dominate the signal on small scales, so even if we could determine the correlation functions there, the results would not be reliable.

criteria and allow the separation of a signal into E-modes E_n and B-modes B_n .

Given the set of filter functions, one can determine the COSEBIs for a set of correlation functions on a finite interval $[\theta_{\min}, \theta_{\max}]$, which is extremely convenient for the analysis of observed data. However, the filter functions $T_{n\pm}$ are rapidly alternating (especially T_{n-} ; each of these functions change sign between θ_{\min} and $2\theta_{\min}$). In order for the numerical errors to be negligible, the shear correlation function ξ_{\pm} needs to be determined in about 10^5 angular bins. While not an easy challenge, cosmological analyses with COSEBIs have been carried out (compare e.g. Asgari et al. 2018; Asgari and Heymans 2019).

The effects of varying depth

In this chapter we will explore the effects of varying depth on different shear statistics. In abstract terms, this is a position-based selection effect: In some places fainter galaxies can not be detected due to higher noise levels, whereas in other places the same galaxies would be detected. This leads to a modification of number density, as in deeper pointings more galaxies can be detected, as well as a modification in the shear statistics themselves, as fainter galaxies are on average located at a higher redshift.

We will be working with data from the KiDS+Viking-450 (KV450) Survey (Wright et al. 2018). The KV450 survey combines data in the *ugri*-band from the Kilo Degree Survey (KiDS) with the *ZYJHK_s*-band imaging from the VISTA Kilo Degree Infrared Galaxy Survey (VIKING) over 458 square degrees. The unprecedented coverage in 9 photometric bins allows a relatively narrow photometric-to-spectroscopic redshift comparison and thus significantly reduces systematic biases arising from incorrect redshift determination.

For the cosmic shear analysis, the galaxies were separated into five tomographic bins of photometric redshift z_b . In the areas where the survey overlaps with spectroscopic surveys, a true redshift distribution was extracted for each of the tomographic bins. A summary of the bin boundaries, the (weighted) number of galaxies¹ in each bin and the average spectroscopic redshifts can be found in Table 3.1. A detailed explanation of the determination of the redshift distributions, the measured correlation functions and the inferred cosmological parameters can be found in Hildebrandt et al. (2017) and Hildebrandt et al. (2018).

While there are many position-based selection effects having similar impacts, like depth in the different colour bands, seeing, airmass, Galactic extinction, dithering strategies and CCD imperfections, we chose

¹ Throughout this thesis, when we speak of the (weighted) number of galaxies in a sample, we refer to the sum of all lensing weights of the galaxies belonging to the respective sample. As all quantities like the average redshift distribution, the shear correlation functions etc. are calculated using this number, it carries way more information than the unweighted number of galaxies. For that reason, whenever we speak of a number of galaxies, unless otherwise specified, we refer to the sum of their respective lensing weights.

Bin	z_b^{\min}	z_b^{\max}	N	$\langle z_{\text{spec}} \rangle$
1	0.1	0.3	386208	0.49
2	0.3	0.5	563719	0.53
3	0.5	0.7	799492	0.69
4	0.7	0.9	532226	0.84
5	0.9	1.2	415980	1.00

Table 3.1 – Minimum photometric redshift z_b^{\min} , maximum photometric redshift z_b^{\max} , weighted number of galaxies N and average spectroscopic redshift $\langle z_{\text{spec}} \rangle$ of the five tomographic redshift bins in the KV450 Survey.

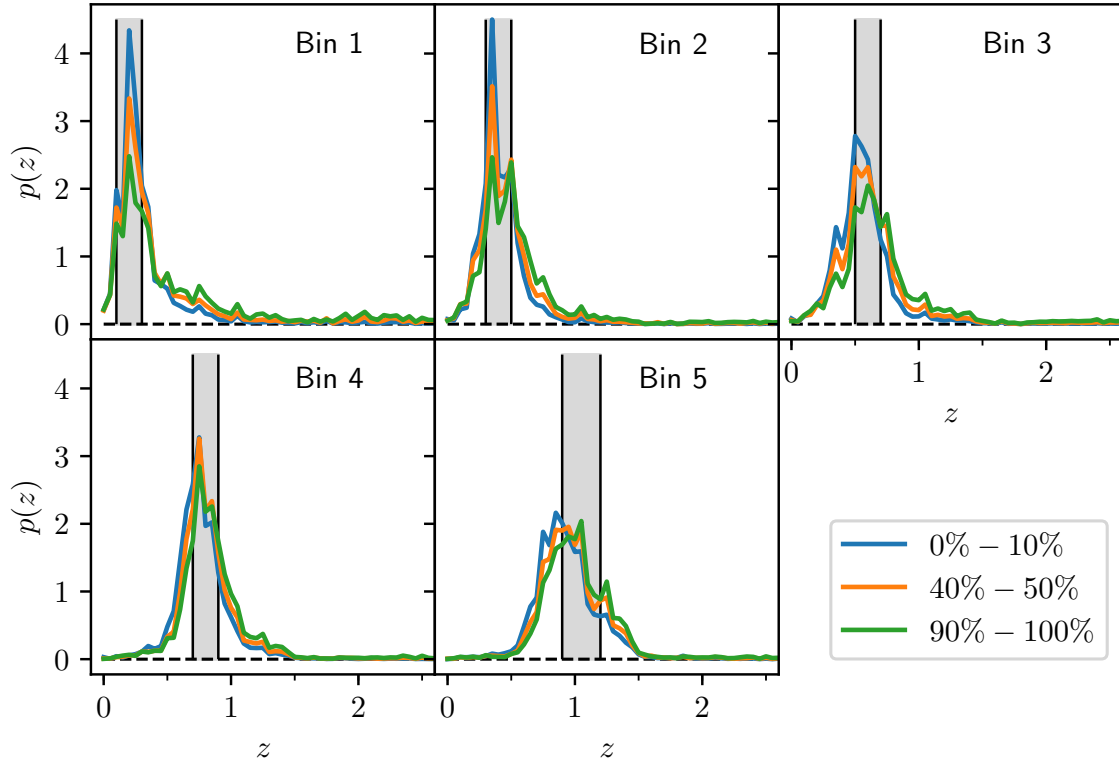


Figure 3.1 – Redshift distribution for the worst, a medium and the best percentile for each tomographic bin. The grey area highlights photometric redshift bin.

to focus on the r -band depth of a pointing. As the r -band served as the detection band, its depth appears to be the most relevant factor. As of now, we ignore the other effects as we expect them to play a subdominant role, but the investigation of those is definitely necessary in further studies.

To estimate the extent of the varying depth between pointings, we received some data by H. Hildebrandt: All pointings were sorted by r -band depth and split into ten percentiles, ordered from shallow to deep. For each of the percentiles of every tomographic bin, the redshift distribution and the weighted number of galaxies were extracted. Inspecting Figure 3.1, one can clearly see that the redshift distribution strongly varies between the percentiles – especially the lower-redshift bins show a significant tail of high-redshift galaxies for deep pointings. It is also noticeable that the spectroscopic redshift distribution of galaxies only roughly traces their photometric redshift bins. While this might seem like a problem, as long as we have a precise knowledge the spectroscopic redshift distribution for Eq. (2.57), this does not affect the results.

Additionally, when we look at Figure 3.2, we notice some interesting features: First and foremost, there is an obvious strong correlation between average redshift and the number of galaxies for all bins. Furthermore, the low redshift bins seem to vary extremely strongly in redshift and only subdominantly in the number of galaxies, whereas the trend is vice versa for the high-redshift bins. This behaviour is easily explained: Almost all galaxies in the low-redshift bins are close (and thus bright) enough for us to detect them, even with suboptimal depth in the pointing. A significant fraction of the galaxies included in

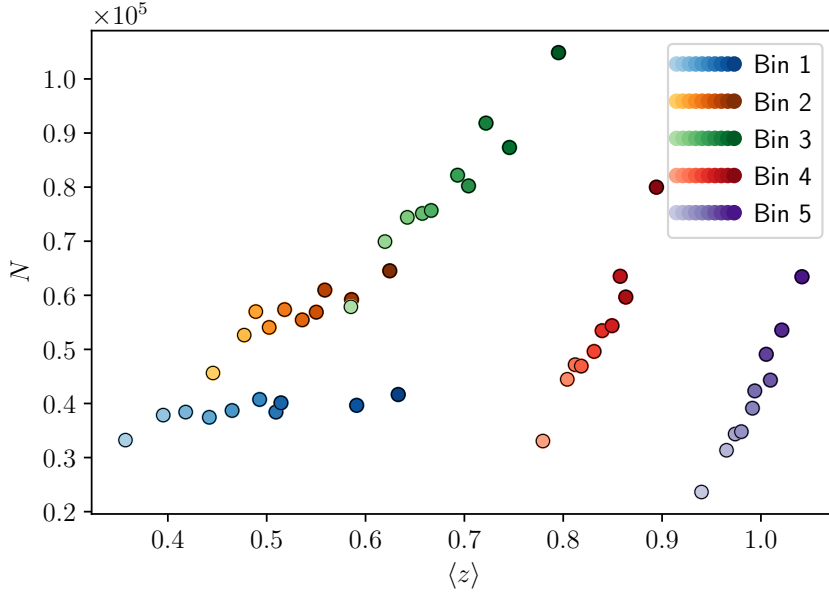


Figure 3.2 – Weighted number of galaxies N as a function of average (spectroscopic) redshift $\langle z \rangle$ for each percentile of the five tomographic bins. Values for this can be found in Table C.1 in the Appendix.

the high percentiles are ones with extremely high ($z \gtrsim 2$) spectroscopic redshift, which leads to a strong increase in average redshift. The galaxies in the high-redshift bins, however, are relatively dim and thus harder to detect. For shallow pointings the number of detected galaxies thus significantly decreases. Still, the additional galaxies detected in deeper pointings do not influence the average redshift that much, as the average redshift is already pretty high.

We see that the r -band depth has a strong effect on the number of detected galaxies as well as on their average redshift. These two effects will definitely influence the measured shear statistics if one does not account for them. In the next two sections we will develop a few models to help us answer the question whether this influence is significant for the results of the KV450 survey, and if it can be detected by analysis of the B-modes.

3.1 Toy model – a single lens plane

For our first analysis we will further simplify our assumptions: We imagine that all the matter between sources and observer is concentrated in a single lens plane of distance D_d from the observer. If we now distribute sources at varying distances D_s , then the convergence κ varies according to $\kappa \propto D_{ds}/D_s$.

Assuming that the survey depth, and thus the source redshift populations, vary between pointings, an observer will measure a shear-signal that is modified by a depth function $W(\theta) = 1 + w(\theta) \propto D_{ds}/D_s$, where $\langle w(\theta) \rangle = 0$ holds. We will model the effects of such a depth function in three different ways - by modelling a convergence field directly, by computing the effects on the power spectrum and by investigating the change of the shear correlation functions.

3.1.1 Modelling a shear field

As a first test, we simulated the convergence κ as a Gaussian random field² and converted it to a shear-field γ via Eq. (2.48). This field was then multiplied by a pointing-based depth function $W(\theta)$. For simplicity we modelled the weighting by random variables from a normal distribution with mean $\mu = 1$ and variance $\sigma = 0.1$. After that, we transformed the shear field back into a convergence field κ^{obs} . The transformations between the fields were done using the convolution theorem. For the Fourier transformations, periodic boundary conditions were asserted. As the observed shear field is modified, the reconstruction of the observed convergence κ^{obs} will not yield the original convergence. In particular, there is no reason why the convolution with a complex kernel should have a nonzero imaginary part. This allows us to separate our received signal into E- and B-modes via Eq. (2.67). As an example, Figure 3.3 shows the procedure for one $4 \times 4 \text{ deg}^2$ -field.

It is interesting to note that the difference in E-modes is predominantly within the 1 deg^2 -fields, whereas the majority of B-modes arise close to the boundaries of each field. However, the reconstructed convergence field is not a good statistic for cosmic shear. Additionally, while the initial density fluctuations might be a Gaussian random field, cosmic shear is measured in the nonlinear regime of structure growth, which no longer takes the form of a Gaussian random field. While this visual inspection serves as a good first start, it is not suitable to make any reliable predictions. For this reason, I chose to investigate two-point shear statistics, namely the power spectrum and the shear correlation functions.

3.1.2 Effects on the power spectrum

For the analysis of the power spectrum we adopt the same pointing-based depth function $\gamma^{\text{obs}}(\theta) = W(\theta)\gamma(\theta)$ with $W(\theta) = 1 + w(\theta)$, where $\langle w(\theta) \rangle = 0$ holds. In accordance to the definition of the shear power spectrum

$$(2\pi)^2 \delta(\ell - \ell') P(|\ell|) = \langle \tilde{\gamma}(\ell) \tilde{\gamma}(\ell') \rangle, \quad (3.1)$$

we define the observed power spectrum via

$$P^{\text{obs}}(\ell) \equiv \frac{1}{(2\pi)^2} \int d^2 \ell' \langle \tilde{\gamma}^{\text{obs}}(\ell) \tilde{\gamma}^{\text{obs}*}(\ell') \rangle. \quad (3.2)$$

Note that due to the depth-function both the assumptions of homogeneity and isotropy break down, which means that we can neither assume isotropy in the power spectrum, nor can we assume that $\langle \tilde{\gamma}^{\text{obs}}(\ell) \tilde{\gamma}^{\text{obs}*}(\ell') \rangle$ vanishes for $\ell \neq \ell'$. In this section we will outline the computation of the observed power spectrum. A more detailed version can be found in Appendix A.1. We compute the correlation of the Fourier transformed observed shear as

$$\begin{aligned} \langle \tilde{\gamma}^{\text{obs}}(\ell) \tilde{\gamma}^{\text{obs}*}(\ell') \rangle &= \left\langle \int d^2 \theta \int d^2 \theta' W(\theta) W(\theta') \gamma(\theta) \gamma^*(\theta') \exp(i\ell \cdot \theta - i\ell' \cdot \theta') \right\rangle \\ &= \left\langle \int \frac{d^2 k}{(2\pi)^2} P(k) \tilde{W}(\ell - k) \tilde{W}^*(\ell' - k) \right\rangle. \end{aligned}$$

² A Gaussian random field is fully characterized by its power spectrum $P(|k|)$. A particular realization is obtained by drawing Gaussian deviates with dispersion $\sigma(k) = \sqrt{P(|k|)}$ for each k , multiplying them with a random phase ϕ_k , and then Fourier transforming the obtained field.

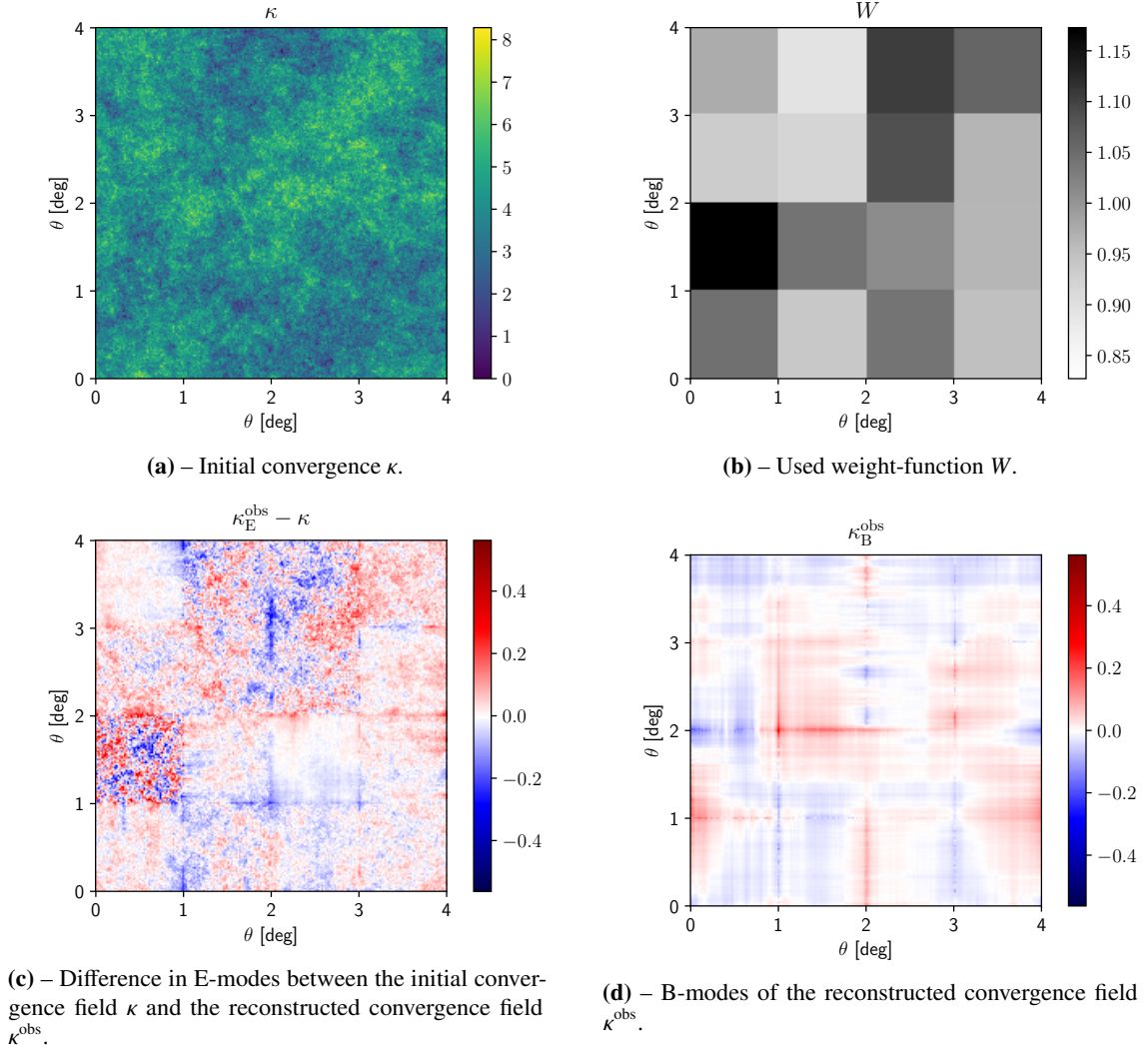


Figure 3.3 – Estimating E- and B-modes of a reconstructed convergence field.

Inserting $W(\boldsymbol{\theta}) = 1 + w(\boldsymbol{\theta})$ we derive

$$\begin{aligned} \langle \tilde{\gamma}^{\text{obs}}(\boldsymbol{\ell}) \tilde{\gamma}^{\text{obs}*}(\boldsymbol{\ell}') \rangle &= \left\langle \int \frac{d^2 k}{(2\pi)^2} P(\mathbf{k}) \left[(2\pi)^4 \delta(\boldsymbol{\ell} - \mathbf{k}) \delta(\boldsymbol{\ell}' - \mathbf{k}) + (2\pi)^2 [\tilde{w}(\boldsymbol{\ell} - \mathbf{k}) \delta(\boldsymbol{\ell}' - \mathbf{k}) \right. \right. \\ &\quad \left. \left. + \tilde{w}^*(\boldsymbol{\ell}' - \mathbf{k}) \delta(\boldsymbol{\ell} - \mathbf{k})] + \tilde{w}(\boldsymbol{\ell} - \mathbf{k}) \tilde{w}(\boldsymbol{\ell}' - \mathbf{k}) \right] \right\rangle \\ &= (2\pi)^2 \delta(\boldsymbol{\ell} - \boldsymbol{\ell}') P(\boldsymbol{\ell}) + \left\langle \int \frac{d^2 k}{(2\pi)^2} \tilde{w}(\boldsymbol{\ell} - \mathbf{k}) \tilde{w}^*(\boldsymbol{\ell}' - \mathbf{k}) P(\mathbf{k}) \right\rangle. \end{aligned}$$

To model an arbitrary depth function that is constant on each individual pointing α , we can choose weights w_α , that only need to satisfy $\langle w_\alpha \rangle = 0$, and parametrize $w(\boldsymbol{\theta})$ as

$$w(\boldsymbol{\theta}) = \sum_{\alpha \in \mathbb{Z}^2} w_\alpha \Xi(\boldsymbol{\theta} - L\alpha), \text{ with the Box-Function } \Xi(\boldsymbol{\theta}) = \begin{cases} 1 & \boldsymbol{\theta} \in \left[-\frac{L}{2}, \frac{L}{2}\right]^2 \\ 0 & \text{else} \end{cases}, \quad (3.3)$$

where L is the length of one pointing. Assuming an uncorrelated distribution for the weight function ($\langle w_\alpha w_\beta \rangle = 0$ for $\alpha \neq \beta$), we define $\langle w^2 \rangle \equiv \langle w_\alpha^2 \rangle$. We can then calculate the observed power spectrum via

$$\begin{aligned} P^{\text{obs}}(\boldsymbol{\ell}) &= \frac{1}{(2\pi)^2} \int d^2 \ell' \langle \tilde{\gamma}^{\text{obs}}(\boldsymbol{\ell}) \tilde{\gamma}^{\text{obs}*}(\boldsymbol{\ell}') \rangle \\ &= P(\boldsymbol{\ell}) + \langle w^2 \rangle \int \frac{d^2 k}{(2\pi)^2} \tilde{\Xi}(\boldsymbol{\ell} - \mathbf{k}) P(\mathbf{k}), \end{aligned} \quad (3.4)$$

where $\tilde{\Xi}$ is the Fourier transform of a box-function, namely a sinc-function.

The observed power spectrum P^{obs} is thus composed of the original power spectrum P , plus a convolution of the power spectrum with a two-dimensional sinc-function, scaling with the variance of the geometric lensing efficiency $\langle \frac{D_{\text{ds}}}{D_s} \rangle$. In particular, the power spectrum is not isotropic anymore. Following Schneider, van Waerbeke and Mellier (2002), it would be interesting to extract E- and B-mode information out of this power spectrum. The B-mode power spectrum for the simulations described in Section 3.1.1, this time for a $20 \times 20 \text{ deg}^2$ -field, can be seen in Figure 3.4. As the B-mode power spectrum is solely created by this effect, the imprint of the sinc-function is clearly visible.

Unfortunately, it is quite difficult to include any form of weighting in the analysis of the power spectrum, both in the form of number density and in the form of lensing weights. We will therefore analyse the change in the shear correlation functions, as these functions allow for a straightforward implementation of weightings. For the E- and B-mode decomposition we will rely on the COSEBIs (Schneider, Eifler and Krause 2010).

3.1.3 The function $E(\boldsymbol{\theta})$

When computing the shear correlation between a pair of galaxies, it is of central importance whether those two galaxies lie in the same pointing or not. We want to model the probability that a pair of galaxies with separation $\boldsymbol{\theta}$ lie in the same pointing by the function $E(\boldsymbol{\theta})$, which we will derive here:

Given one square field of length L (in our case $L = 60'$) and a separation vector $\boldsymbol{\theta}$, without loss of generality we can assume $\theta_1, \theta_2 \geq 0$. As depicted in Figure 3.5, the dashed square represents all possible positions that the first galaxy can take, such that the second galaxy is still within the same pointing. The

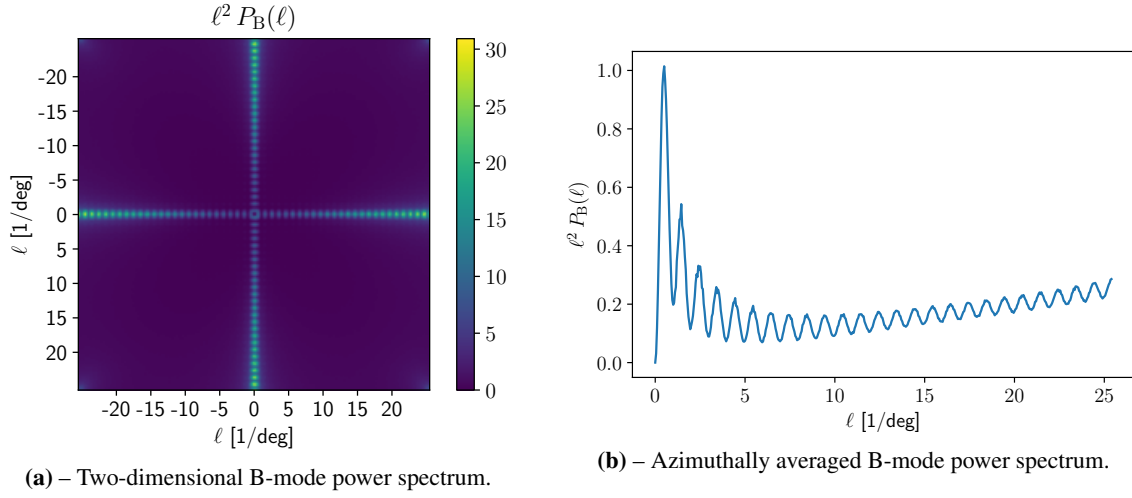


Figure 3.4 – One- and two-dimensional B-mode power spectra for simulations of Gaussian random fields.

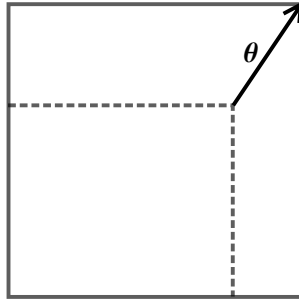


Figure 3.5 – Graphic representation on how to obtain the function $E(\theta)$. For a separation vector θ , the dashed square represents the area of galaxies that have their partner in the same pointing.

volume of this square equals

$$V(|\theta|, \phi) = [L - |\theta| \cos(\phi)] [L - |\theta| \sin(\phi)], \quad (3.5)$$

where ϕ represents the angle of the vector θ . The function $E(\theta)$ then simply equals $V(|\theta|, \phi)/L^2$. To exclude negative Volumes (which could occur when $|\theta| > 1$ holds), we need to add the Heaviside theta function \mathcal{H} :

$$E(\theta) = \left[1 - \frac{|\theta|}{L} \cos(\phi)\right] \left[1 - \frac{|\theta|}{L} \sin(\phi)\right] \mathcal{H}\left[1 - \frac{|\theta|}{L} \cos(\phi)\right] \mathcal{H}\left[1 - \frac{|\theta|}{L} \sin(\phi)\right]. \quad (3.6)$$

As $E(\theta)$ is not isotropic, in order to obtain the function $E(\theta) = E(|\theta|)$, we need to azimuthally average Equation (3.6) over all angles ϕ . While the case $\theta_1, \theta_2 \geq 0$ certainly does not hold for all angles ϕ , we

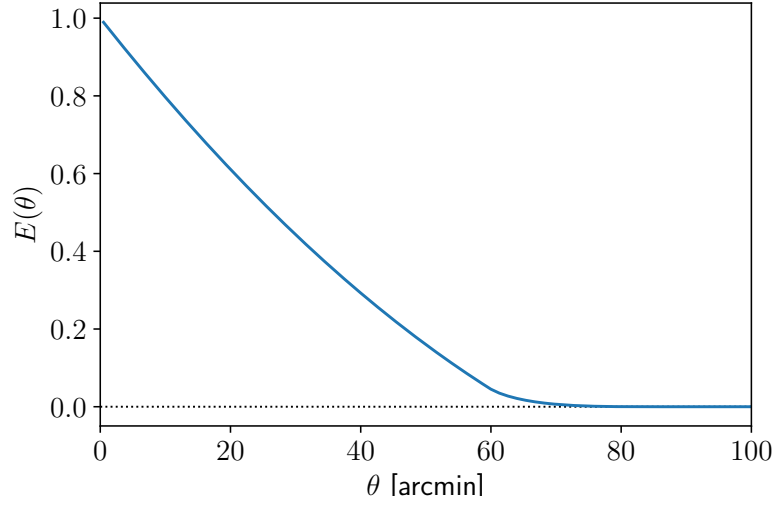


Figure 3.6 – Probability that a random pair of galaxies of separation θ lie in the same pointing.

can eliminate the other cases by simple symmetry.

$$\begin{aligned}
 E(\theta) &= \frac{4}{2\pi} \int_0^{\frac{\pi}{2}} d\phi E(\theta) = \frac{2}{\pi} \begin{cases} \int_0^{\frac{\pi}{2}} d\phi \left[1 - \frac{|\theta|}{L} \cos(\phi) \right] \left[1 - \frac{|\theta|}{L} \sin(\phi) \right], & |\theta| \leq L \\ \int_{\cos^{-1}(L/|\theta|)}^{\sin^{-1}(L/|\theta|)} d\phi \left[1 - \frac{|\theta|}{L} \cos(\phi) \right] \left[1 - \frac{|\theta|}{L} \sin(\phi) \right], & L \leq |\theta| \leq \sqrt{2}L \\ 0, & \sqrt{2}L \leq \theta \end{cases} \\
 &= \begin{cases} \frac{1}{L^2\pi} [L^2\pi - (4L - \theta)\theta], & \theta \leq L \\ \frac{2}{\pi} \left[4 \sqrt{\frac{\theta^2}{L^2} - 1} - 1 - \frac{\theta^2}{2L^2} - \cos^{-1}\left(\frac{L}{\theta}\right) + \sin^{-1}\left(\frac{L}{\theta}\right) \right], & L \leq \theta \leq \sqrt{2}L \\ 0, & \sqrt{2}L \leq \theta \end{cases} \quad (3.7)
 \end{aligned}$$

The function is depicted in Figure 3.6.

3.1.4 Modelling the shear correlation functions

For a first simple analysis we will assume that a deeper redshift distribution just yields a stronger shear signal, in the sense that the shear field for a deeper redshift distribution gets multiplied by a weight W . While this is not true for a 3-dimensional matter distribution, it should be valid for small variations in redshift. Additionally, we assume that a higher depth does not only lead to a stronger average shear, but also to a higher galaxy number density, implying a correlation between those two quantities.

Let $N^i(\theta)$, $N^j(\theta)$ be the average weighted number of galaxies per pointing in redshift bins i and j and let $W^i(\theta)$, $W^j(\theta)$ be the weighting of average shear. The observed correlation function $\xi_{\pm}^{ij, \text{obs}}(\theta)$ now

changes from one of constant depth $\xi_{\pm}^{ij,\text{const}}(\theta)$ via (compare Eq. 2.63)

$$\begin{aligned}\xi_{\pm}^{ij,\text{obs}}(\theta) &= \frac{\langle N^i(\theta')N^j(\theta' + \theta)\gamma_t^{i,\text{obs}}(\theta')\gamma_t^{j,\text{obs}}(\theta' + \theta) \rangle}{\langle N^i(\theta')N^j(\theta' + \theta) \rangle} \pm \frac{\langle N^i(\theta')N^j(\theta' + \theta)\gamma_{\times}^{i,\text{obs}}(\theta')\gamma_{\times}^{j,\text{obs}}(\theta' + \theta) \rangle}{\langle N^i(\theta')N^j(\theta' + \theta) \rangle} \\ &= \frac{\langle N^i(\theta')N^j(\theta' + \theta)W^i(\theta')W^j(\theta' + \theta) \rangle}{\langle N^i(\theta')N^j(\theta' + \theta) \rangle} \left(\langle \gamma_t^i(\theta')\gamma_t^j(\theta' + \theta) \rangle \pm \langle \gamma_{\times}^i(\theta')\gamma_{\times}^j(\theta' + \theta) \rangle \right) \\ &= \frac{\langle N^i(\theta')N^j(\theta' + \theta)W^i(\theta')W^j(\theta' + \theta) \rangle}{\langle N^i(\theta')N^j(\theta' + \theta) \rangle} \xi_{\pm}^{ij,\text{const}}(\theta),\end{aligned}\quad (3.8)$$

where the average $\langle \dots \rangle$ represents both an ensemble average as well as an average over the position θ' . Assuming that depth and galaxy number density of neighbouring pointings are uncorrelated, the only important property of a galaxy pair is whether or not they lie in the same pointing, which is described by the function $E(\theta)$.

To compute the modified shear correlation functions, we parametrize the number densities $N^i(\theta) = \langle N^i \rangle [1 + n^i(\theta)]$ and the weight $W^i(\theta) = 1 + w^i(\theta)$ and, as in (3.3), interpret $n^i(\theta)$ as a function with average $\langle n^i \rangle = 0$, that is constant on each pointing. Inspecting Eq. (3.8), without loss of generality we can set $\langle N^i \rangle = 1$, as this term appears both in numerator and denominator. We can see that $\langle n^i(\theta')n^j(\theta' + \theta) \rangle = E(\theta) \langle n^i(\theta')n^j(\theta') \rangle \equiv E(\theta) \langle n^i n^j \rangle$ holds and compute:

$$\begin{aligned}&\langle N^i(\theta')N^j(\theta' + \theta)W^i(\theta')W^j(\theta' + \theta) \rangle \\ &= \langle [1 + n^i(\theta')] [1 + n^j(\theta' + \theta)] [1 + w^i(\theta')] [1 + w^j(\theta' + \theta)] \rangle \\ &= 1 + \langle n^i(\theta')n^j(\theta' + \theta) \rangle + \langle n^i(\theta')w^i(\theta') \rangle + \langle n^i(\theta')w^j(\theta' + \theta) \rangle + \langle n^j(\theta' + \theta)w^i(\theta') \rangle \\ &\quad + \langle n^j(\theta' + \theta)w^j(\theta' + \theta) \rangle + \langle w^i(\theta')w^j(\theta' + \theta) \rangle + \langle n^i(\theta')n^j(\theta' + \theta)w^i(\theta') \rangle \\ &\quad + \langle n^i(\theta')n^j(\theta' + \theta)w^j(\theta' + \theta) \rangle + \langle n^i(\theta')w^i(\theta')w^j(\theta' + \theta) \rangle + \langle n^j(\theta' + \theta)w^i(\theta')w^j(\theta' + \theta) \rangle \\ &\quad + \langle n^i(\theta')n^j(\theta' + \theta)w^i(\theta')w^j(\theta' + \theta) \rangle \\ &= 1 + \langle n^i w^i \rangle + \langle n^j w^j \rangle + E(\theta) [\langle n^i n^j \rangle + \langle n^i w^j \rangle + \langle n^j w^i \rangle + \langle w^i w^j \rangle + \langle n^i n^j w^i \rangle + \langle n^i n^j w^j \rangle + \langle n^i w^i w^j \rangle \\ &\quad + \langle n^j w^i w^j \rangle + \langle n^i n^j w^i w^j \rangle]\end{aligned}\quad (3.9)$$

Ignoring correlations higher than second order³, and performing the same calculation for the denominator of Eq. (3.8), we get

$$\xi_{\pm}^{ij,\text{obs}}(\theta) = \frac{1 + \langle n^i w^i \rangle + \langle n^j w^j \rangle + E(\theta) [\langle n^i n^j \rangle + \langle n^i w^j \rangle + \langle n^j w^i \rangle + \langle w^i w^j \rangle]}{1 + E(\theta) \langle n^i n^j \rangle} \xi_{\pm}^{ij,\text{const}}(\theta). \quad (3.10)$$

We see that in addition to a modification of the correlation function due to the stronger shear signal in deeper pointings, we also get a scale-independent modification due to the correlation between depth and number density.

For the calculation of the reference correlation functions $\xi_{\pm}^{ij}(\theta)$ we distribute the *same* galaxies into

³ Assuming n and w are small, this is a valid approximation. However, inspecting Figure 3.2, we see that this assumption is not necessarily valid. However, we performed both calculations for the KV450-survey and found no significant difference.

our survey, only this time we will not order their weightings W or their number densities N by pointing. We can imagine this by cutting the footprint into infinitesimal elements $d^2\theta$, and redistributing those at random. When we calculate the correlation function of this survey, we note that $\langle n^i(\theta') \rangle \langle n^j(\theta' + \theta) \rangle = 0$ holds for $\theta \neq 0$, as the two corresponding infinitesimal elements have uncorrelated weighting and number density. We again calculate

$$\xi_{\pm}^{ij}(\theta) = \frac{\langle N^i(\theta') N^j(\theta' + \theta) W^i(\theta') W^j(\theta' + \theta) \rangle}{\langle N^i(\theta') N^j(\theta' + \theta) \rangle} \xi_{\pm}^{ij, \text{const}}(\theta), \quad (3.11)$$

only this time, as weight and number density between different positions are uncorrelated, the denominator of Eq. (3.11) is unity and the numerator is

$$\langle [1 + n^i(\theta')] [1 + n^j(\theta' + \theta)] [1 + w^i(\theta')] [1 + w^j(\theta' + \theta)] \rangle = 1 + \langle n^i w^i \rangle + \langle n^j w^j \rangle. \quad (3.12)$$

This yields a relation between the correlation function of constant optical depth $\xi_{\pm}^{ij, \text{const}}$ and the modelled one ξ_{\pm}^{ij} :

$$\xi_{\pm}^{ij}(\theta) = \left(1 + \langle n^i w^i \rangle + \langle n^j w^j \rangle\right) \xi_{\pm}^{ij, \text{const}}(\theta). \quad (3.13)$$

The ratio of modelled and observed correlation function thus becomes:

$$\begin{aligned} \frac{\xi_{\pm}^{ij}(\theta)}{\xi_{\pm}^{ij, \text{obs}}(\theta)} &= \frac{(1 + \langle n^i w^i \rangle + \langle n^j w^j \rangle)(1 + E(\theta) \langle n^i n^j \rangle)}{1 + \langle n^i w^i \rangle + \langle n^j w^j \rangle + E(\theta) [\langle n^i n^j \rangle + \langle n^i w^j \rangle + \langle n^j w^i \rangle + \langle w^i w^j \rangle]} \\ &\approx \frac{1 + \langle n^i w^i \rangle + \langle n^j w^j \rangle + E(\theta) \langle n^i n^j \rangle}{1 + \langle n^i w^i \rangle + \langle n^j w^j \rangle + E(\theta) [\langle n^i n^j \rangle + \langle n^i w^j \rangle + \langle n^j w^i \rangle + \langle w^i w^j \rangle]}. \end{aligned} \quad (3.14)$$

It is interesting to note that $\xi_{\pm}^{ij} = \xi_{\pm}^{ij, \text{obs}}$ holds wherever $E(\theta) = 0$, meaning that the correlation function is not affected for large angular scales. Given a set of average redshifts, following Van Waerbeke et al. (2006), we can estimate

$$\langle |\gamma| \rangle \propto \langle z \rangle^{0.85}. \quad (3.15)$$

We shall later see that this approximation is valid for higher tomographic redshift bins $z \gtrsim 0.5$, but starts to break down at lower redshifts. We thus want to construct a model that is valid for an arbitrary distribution of redshifts and does not rely on the assumption of a single lens plane.

3.2 Semi-analytical model for the shear correlation functions

The analysis of data from the Kilo-Degree Survey showed that the redshift-distribution of sources was highly correlated with the depth in the r -band. We thus chose to separate the survey into 10 percentiles, sorted by r -band depth, meaning that if a pointing had a worse depth than 90% of the other pointings, it would belong to the first percentile, and so on. Now for each percentile m and each tomographic redshift bin i we can extract a weighted number of galaxies N_m^i and, in case the pointing overlaps with a spectroscopic survey, a source redshift distribution $p_m^i(z)$. Using (2.61), we can compute the shear correlation functions $\xi_{\pm, mn}^{ij}(\theta)$ for each set of percentiles m, n and redshift bins i, j ⁴. When we compute

⁴ For the calculation of the shear correlation functions we use the NICA EA-program. Among other things, it calculates the shear correlation functions for a given cosmology and source redshift distribution. To estimate the power spectrum on nonlinear

the measured shear correlation functions of a survey, we take the weighted average of tangential and cross shears of all pairs of galaxies (Hildebrandt et al. (2017) give a good overview for the process). If, for a single pair of galaxies, one galaxy lies in the m -th percentile of redshift bin i and the second one lies in the n -th percentile of redshift bin j , then their contribution to the observed correlation functions is, on average, $\xi_{\pm, mn}^{ij}(\theta)$. This means that if we know each of those single correlation functions, we can reconstruct the total correlation functions via a weighted average of the single functions. Formally, we define

$$\xi_{\pm}^{ij, \text{obs}}(\theta) = \frac{\sum_{m,n} P_{mn}^{ij}(\theta) \xi_{\pm, mn}^{ij}(\theta)}{\sum_{m,n} P_{mn}^{ij}(\theta)}, \quad (3.16)$$

where P_{mn}^{ij} is the new weighting of the correlation functions. This weighting has to be proportional to the probability that a galaxy pair of distance θ is of percentiles m and n , as well as to the original weighting of these galaxies.

For $m \neq n$ we know that the pair of galaxies has to lie in different pointings, which is accounted for by including the factor $[1 - E(\theta)]$. Furthermore, the first galaxy has to lie in percentile m , the probability of which we will denote with $P(m)$. As we have 10 different percentiles, and average over the whole footprint of the survey, $P(m) = 1/10$ holds. When the first pointing is of percentile m , we want to denote the probability that a galaxy in a different pointing with distance θ is of percentile n by $P(n|m, \theta)$. The impact of such a galaxy pair on the correlation functions scales with the product of the weighted number of galaxies N_m^i, N_n^j . We get for $n \neq m$:

$$P_{mn}^{ij}(\theta) = [1 - E(\theta)] \frac{1}{10} P(n|m, \theta) N_m^i N_n^j. \quad (3.17)$$

For the calculation of $P_{mm}^{ij}(\theta)$ we have to account for a different possibility: In case that the galaxy lies in the same pointing [accounted for by the factor $E(\theta)$], it automatically is of the same percentile. We therefore set

$$P_{mm}^{ij}(\theta) = E(\theta) \frac{1}{10} N_m^i N_m^j + [1 - E(\theta)] \frac{1}{10} P(m|m, \theta) N_m^i N_m^j. \quad (3.18)$$

In our case, we assume an uncorrelated distribution of percentiles, such that we can set $P(n|m, \theta) = 1/10$. We can then write $P_{mn}^{ij}(\theta)$ as:

$$P_{mn}^{ij}(\theta) = E(\theta) \frac{1}{10} N_m^i N_n^j \delta_{mn} + [1 - E(\theta)] \frac{1}{100} N_m^i N_m^j, \quad (3.19)$$

where δ_{mn} denotes the Kronecker delta. Inserting this into Eq. (3.16), we compute

$$\xi_{\pm, mn}^{ij, \text{obs}}(\theta) = \frac{1}{C} \sum_{m=1}^{10} N_m^i \left\{ E(\theta) N_m^j \xi_{\pm, mm}^{ij}(\theta) + \frac{[1 - E(\theta)]}{10} \sum_{n=1}^{10} N_n^j \xi_{\pm, mn}^{ij}(\theta) \right\}, \quad (3.20)$$

with the normalization

$$C = \sum_{m=1}^{10} N_m^i \left[E(\theta) N_m^j + \frac{[1 - E(\theta)]}{10} \sum_{n=1}^{10} N_n^j \right]. \quad (3.21)$$

A more mathematically rigorous derivation of this function can be found in Appendix A.2.

If we want to compute this for all 5 redshift bins of the KV450-survey, this forces us to calculate 1275 correlation functions and add them, thus yielding potential numerical errors (apart from being

scales we use the methods developed by Takahashi et al. (2012).

computationally expensive). However, if we examine Eq. (2.56), we see that the comoving distance distribution of sources factors in linearly. This in turn implies that in Equations (2.57) and (2.61) both source distance distributions factor in linearly. This basically means that, instead of adding correlation functions, we can add their respective redshift distributions and compute the correlation functions of that. In particular, we can define the *combined number of galaxies* N^i and *average redshift distribution* $p^i(z)$ of tomographic bin i as

$$N^i \equiv \sum_m N_m^i, \quad p^i(z) = \frac{\sum_m N_m^i p_m^i(z)}{\sum_m N_m^i}. \quad (3.22)$$

If we define ξ_{\pm}^{ij} as the correlation functions between the average redshift distributions $p^i(z)$ and $p^j(z)$, then we observe:

$$\sum_{m,n} N_m^i N_n^j \xi_{\pm,mm}^{ij} = N^i N^j \xi_{\pm}^{ij}. \quad (3.23)$$

Consequently, we can apply this to (3.20), yielding

$$\xi_{\pm}^{ij,\text{obs}}(\theta) = \frac{1}{C} \left\{ E(\theta) \left[\sum_{m=1}^{10} N_m^i N_m^j \xi_{\pm,mm}^{ij}(\theta) \right] + \frac{[1 - E(\theta)]}{10} \xi_{\pm}^{ij}(\theta) N^i N^j \right\}. \quad (3.24)$$

For each set of redshift bins we thus only have to compute eleven correlation functions, which reduces the number of functions to compute from 1275 to 165. We can see that for large distances θ , such that $E(\theta) = 0$ holds, we have $C = N^i N^j$ and thus

$$\xi_{\pm}^{ij,\text{obs}}(\theta) = \frac{1}{N^i N^j} \xi_{\pm}^{ij}(\theta) N^i N^j = \xi_{\pm}^{ij}(\theta), \quad (3.25)$$

so on large scales our observed correlation functions agree with the ones that we would usually calculate.

Results

In the previous chapter we discussed two methods to model the shear correlation functions – an analytic model, that simply relies on the correlations between number density and average redshift, as well as their respective variances, was introduced in Section 3.1.4, whereas a more sophisticated model, that relies on the computation of the correlation functions from different redshift distributions, was discussed in Section 3.2. Both of these methods can be applied to data extracted from the KV450 survey, as outlined in the beginning of Chapter 3.

Furthermore, we appreciate to have received some data from Catherine Heymans, who conducted numerical simulations investigating the same issue: A 100 deg^2 field in the Scinet Light Cone Simulations (SLICS) (Harnois-Déraps et al. 2018) was randomly separated into 10 percentiles. For each tomographic redshift bin of each percentile, galaxies were placed to trace the respective redshift distribution. Afterwards, their expected shear was determined (shape-noise in the form of intrinsic ellipticities of galaxies was not included). This was compared to a set of simulations where the galaxies were simply distributed according to the combined redshift distribution of each respective tomographic bin.

In Figure 4.1 we can see a plot of the ratios between the modelled and observed correlation functions for each of the three methods. It is interesting to note that for the higher redshift bins, the analytic and semi-analytic methods seem to agree on the whole range of θ . However, especially for ξ_- , the lower redshift bins show a significant discrepancy between those two methods, which is expected: The power-law $\langle |\gamma| \rangle \propto z^{0.85}$ inspired by Van Waerbeke et al. (2006) is redshift-dependent and thus not valid for all tomographic bins. Furthermore, especially the lower tomographic bins experience a strong variation in average redshift, whereas the simple model is only valid for small variations in redshift.

We also observe that in the semi-analytic model, ξ_- seems to be much stronger affected by this effect. We can explain this by investigating Figure 2.3: Following Equation (2.61), ξ_+ is computed by filtering the power spectrum with the 0-th order Bessel function. This function peaks at $\ell\theta = 0$, meaning that for all values of θ , the correlation function ξ_+ is sensitive to small values of ℓ , corresponding to large separations θ . However, ξ_- is obtained by filtering with the 4-th order Bessel function, which peaks at approximately $\ell\theta \approx 5$, so for different θ this function is sensitive to varying parts of the convergence power spectrum. A more detailed analysis of this can be found in the Appendix of Köhlinger et al. (2017).

The simulations seem to be in rough agreement with the models, but there are some significant differences. After a thorough analysis we explain these discrepancies the following way: The simulations were performed on a 100 deg^2 field, which means that shot-noise of the fields plays a significant role. After performing the same simulations for a different distribution of depth between the pointings and obtaining completely different results, we are quite certain that this is the dominating effect. The implications of this and possible mitigation strategies will be discussed in Chapter 5.

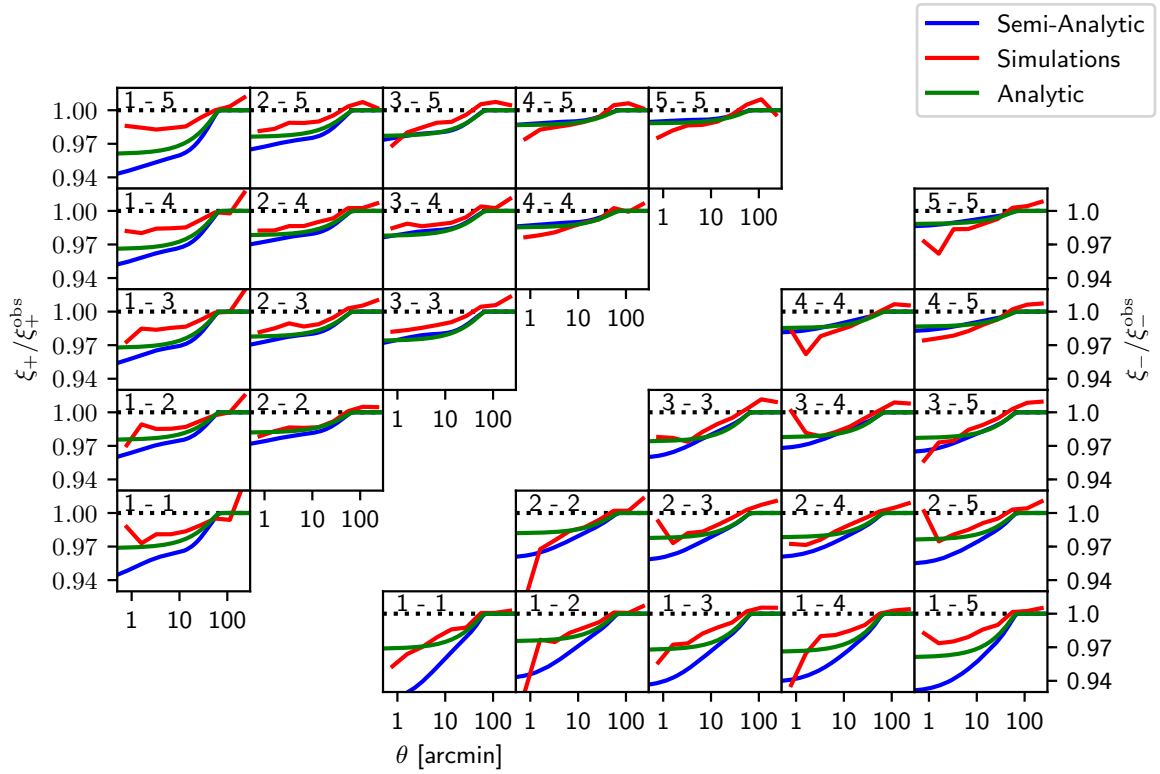


Figure 4.1 – The ratio of modelled to observed correlation functions for the analytic method (green), the semi-analytic method (blue) and the numerical simulations (red) for a cross-correlation of all redshift bins. The upper left triangle shows the ratios for ξ_+ , the lower right triangle the ones for ξ_- . The numbers in the plots denote the respective bins.

To estimate the effects on the cosmological parameters, we performed a Markov-Chain-Monte-Carlo (MCMC) simulation. Given a fiducial cosmology, we calculated a reference set of correlation functions and divided them by the ratios plotted in Figure 4.1, to simulate an observed correlation function. We then calculated sets of correlation functions for different cosmologies and computed the difference to the reference functions, weighted by the respective elements in the inverse covariance matrix C^{-1} of the correlation functions, which was determined by Hildebrandt et al. (2018). The code for this method is a modified version of work by Jan Luca van den Busch.

As our main interest is the investigation of the parameter S_8 , we chose to limit our analysis to the $\Omega_m - \sigma_8$ plane. For the KV450 survey we saw a slight change in the results for Ω_m and σ_8 , but it was far from being relevant. To estimate the impact for the upcoming Euclid-survey we divided the covariance matrix C by 30, to account for the increased survey area¹. In these simulations we saw a bias of about 1σ both for Ω_m and σ_8 . Curiously, both parameters changed in a way such that the parameter S_8 stayed unbiased. The exact values determined by the MCMC simulations can be found in Table 4.1, the likelihood functions can be found in Figures C.1 and C.2 in the Appendix.

As the next step we wanted to investigate the B-modes created by this effect. For this we decided to use the COSEBIs discussed in Section 2.2.3. As the COSEBIs separate E- and B-modes based on a finite interval $[\theta_{\min}, \theta_{\max}]$, they are convenient to use for real data. As varying depth modifies the correlation functions on scales from $0'$ to roughly $85'$, we chose our interval as $\theta_{\min} = 0.5'$ and $\theta_{\max} = 100'$ to be

¹ We want to stress that this is in no way a valid forecast for the Euclid survey. However, we are positive that the qualitative question whether this effect will be relevant, can be answered using this method.

Table 4.1 – Parameter constraints from the MCMC simulations for a KiDS-like and a ‘Euclid-like’ survey subject to varying depth.

	Ω_m	σ_8	S_8
Fiducial	0.250	0.849	0.775
KiDS-like	$0.290^{+0.045}_{-0.091}$	$0.80^{+0.14}_{-0.14}$	$0.763^{+0.044}_{-0.027}$
‘Euclid-like’	$0.264^{+0.011}_{-0.013}$	$0.828^{+0.025}_{-0.025}$	$0.7759^{+0.0067}_{-0.0059}$

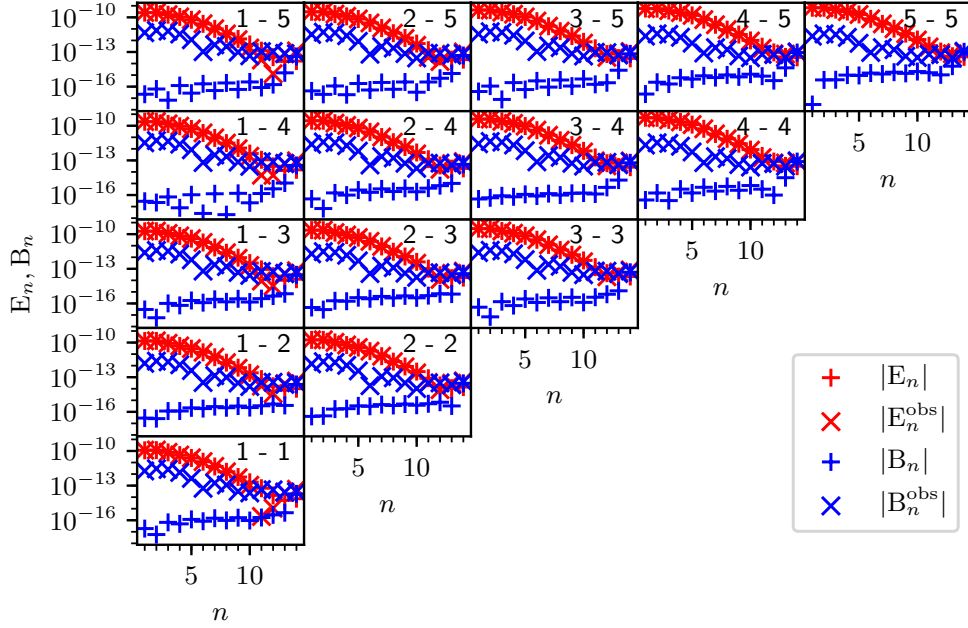


Figure 4.2 – Logarithmic E- and B-modes of the reference and the observed correlation functions for an angular range of $\theta_{\min} = 0.5'$, $\theta_{\max} = 100'$.

especially sensitive to this effect. We calculated the logarithmic COSEBIs (compare Schneider, Eifler and Krause 2010) for a reference set of correlation functions ξ_{\pm} and a set of correlation functions simulating the observed ones, ξ_{\pm}^{obs} . To minimize numerical errors, we determined both correlation functions in 10^6 angular bins. The E- and B-modes determined by this analysis can be seen in Figure 4.2. As the reference correlation functions should not show any B-modes, they serve as an estimate for the numerical errors. As one can see, those errors are several orders of magnitude lower than the determined E- and B-modes for low n , but they rise with increasing n . This is not surprising, as for higher n the filter functions $T_{\pm,n}$ from Equation (2.67) oscillate faster and are thus more prone to numerical errors. As Asgari et al. (2018) pointed out, ξ_{\pm} are relatively smooth functions and are thus already pretty well constrained by the first few E-modes. This is the reason why the E-modes start to rapidly drop for higher n . The B-modes, however, can have more complicated origins, so that they do not necessarily drop as quickly for higher modes. Due to that, for high n the B-modes actually surpass the E-modes.

When we focus on the difference between reference and observed modes (depicted in Figure 4.3), we notice that the difference in E-modes is roughly as high as the one in the B-modes (where the B-modes

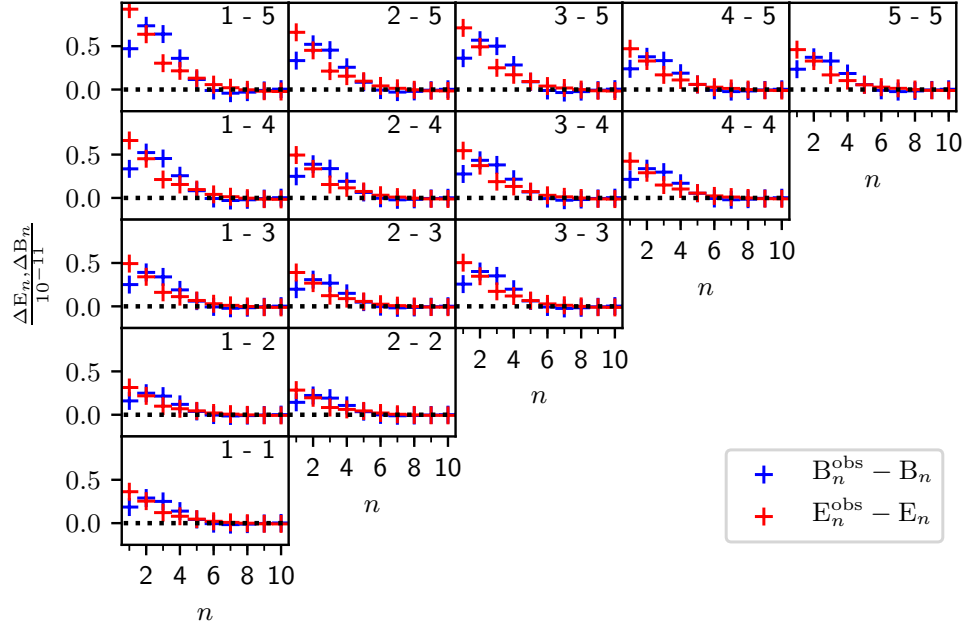


Figure 4.3 – Difference in the logarithmic E- and B-modes between the reference and the observed correlation functions for an angular range of $\theta_{\min} = 0'.5$, $\theta_{\max} = 100'$.

of the reference function are zero). We also notice that both the E-modes and the B-modes show a characteristic pattern that is consistent throughout all redshift bins.

Discussion and conclusion

In this thesis, we have analysed the effects of varying depth on different shear statistics. We started with the simplest case of Gaussian random fields being modified by a weight function with weights following a normal distribution, and then gradually moved on to more realistic cases. There are, however, a few simplifications that we could not get rid of. In this chapter, we will discuss the remaining assumptions and their impact on the results.

1. In the most general terms, we are analysing the effects of a position-based selection function on cosmic shear surveys. In our analysis, this selection function was governed by the r -band depth of a pointing. This neglects a number of other effects: The depth in different bands and the seeing of a pointing will also modify the number densities and redshift distributions on the scale of a pointing, whereas dithering strategies as well as imperfections in the telescope and CCD cause modifications on sub-pointing scales. However, we believe that these effects are subdominant compared to the variations caused by the r -band depth.
2. We have assumed an infinitely large survey area with an uncorrelated distribution of the depth-function. While the boundary effects arising from a finite survey footprint would have a small impact on the shape of the function $E(\theta)$ ¹, the governing factor is the shot noise of the depth-distribution. We have assumed that the probability that a neighbouring pointing is of percentile n is exactly the expectation value, namely $1/10$. While this is true for an infinitely large survey with an uncorrelated distribution of the depth-function, Figure 4.1 clearly shows that it is not valid for a 100 deg^2 field. Whether our assumption holds true for the 450 deg^2 footprint of the KV450 survey, or even the 1350 deg^2 footprint of the final survey is an important question. Also, we have assumed an uncorrelated distribution of the depth-function, both in the simulations as well as in the models. While this is likely true as a rough approximation (very few pointings of the survey were taken on the same night and thus under the same weather conditions), effects like airmass, lunar phase, Galactic extinction and seasonal weather are likely to influence the depth on scales larger than one pointing.

These effects, however, can be mitigated: When investigating Equations (3.17) and (3.18), we see that $P(m|n, \theta)$ denotes the probability that when one galaxy of a pair is in percentile n , then the second galaxy, in a different pointing, is of percentile m . We set this to $1/10$, but a more sophisticated approach is possible here: One can construct functions, similar to $E(\theta)$, representing the probability that the galaxy is in a neighbouring pointing in a certain direction. Then one can

¹ This would be due to the fact that a pointing next to a boundary has less neighbours, therefore making it more likely that a galaxy pair is in the same pointing.

construct the probability distribution that this exact neighbouring pointing is of percentile m , given the actual survey footprint. This mitigates boundary effects, finite field effects and a correlated distribution of depth-functions and should thus be done in future analysis. An outlook to this and a few examples are given in Appendix B. As a preliminary result we find that finite field effects are not significant for a 450 deg^2 or 1000 deg^2 -field, if the distribution of depth is uncorrelated.

3. In our MCMC simulations we did not account for degeneracies with other cosmological parameters or observational effects. Especially intrinsic alignments and baryonic feedback also modify the correlation functions especially on small scales, so they are probably degenerate with the effect of varying depth. In an actual MCMC simulation that accounts for these effects, we suspect that the parameters for intrinsic alignments and baryonic feedback change to mitigate this effect, and the impact on cosmological parameters is actually smaller than in our results. Also, possible degeneracies between S_8 and other cosmological parameters might bias the resulting values.

Despite these repercussions, we are confident to say that the effects of varying depth are not significant for the KV450 survey. The cosmological parameters did not change significantly and the main parameter, S_8 , is especially robust against this effect. In particular this means that a varying depth can not explain the discrepancy between observations of the local Universe and results from analysis of the CMB.

We have shown that this effect can create B-modes. However, Asgari et al. (2018) measured the B-modes of the KV450 survey in the same θ -range. Those B-modes are at least one order of magnitude larger and still consistent with zero, so it is safe to say that the modes created by varying depth are negligible. An interesting observation is that the change in E-modes is as big as the created B-modes (compare Figure 4.3). This means that as soon as this effect causes significant biases in the cosmological parameters, it will also create significant B-modes². Additionally, the created pattern is very characteristic, which makes it easy to recognize in a B-mode analysis of an actual survey.

For next-generation surveys like Euclid, this effect will be significant. Although Euclid is a space-based telescope, the photometric redshift determination will still be done by ground-based telescopes and therefore suffer from the same effects. While this thesis in no way serves as a quantitative study of this effect for Euclid, it does indicate that a such a study should be conducted.

As an outlook it would be interesting to perform a full MCMC simulation, including both cosmological and nuisance parameters. One might also check the most popular extensions to the standard model of cosmology, and see whether varying depth could cause a bias towards one of these models. Furthermore, the method developed in Appendix B could be applied to the actual footprint of the KV450 survey to see whether finite field effects or a correlated distribution of r -band depth are significant. Additionally is interesting to note that $E(\theta)$ is the azimuthal average of the function $E(\boldsymbol{\theta})$, which is not isotropic. Therefore, it would be possible to observe a direction-dependent correlation function $\xi_{\pm}^{ij,\text{obs}}(\boldsymbol{\theta})$ in future surveys. An anisotropy in the observed correlation function could be a sign for the influence of varying depth.

² While this is no big surprise, it is not trivial. It could be possible that a systematic effect only creates E-modes and no B-modes, which would be extremely unfortunate as it could bias cosmological parameters without ever being detected by a B-mode analysis.

Bibliography

- Addison, G. E. et al. (2016), *Quantifying Discordance in the 2015 Planck CMB Spectrum*, *ApJ* **818**, 132 132, arXiv: 1511.00055 (cit. on p. 1).
- Asgari, M. and C. Heymans (2019), *Dark Energy Survey Year 1: An independent E/B-mode cosmic shear analysis*, *MNRAS* **484** L59, arXiv: 1811.10596 (cit. on p. 17).
- Asgari, M. et al. (2018), *Consistent cosmic shear in the face of systematics: a B-mode analysis of KiDS-450, DES-SV and CFHTLenS*, arXiv e-prints, arXiv: 1810.02353 (cit. on pp. 1, 17, 33, 36).
- Bartelmann, M. and P. Schneider (2001), *Weak gravitational lensing*, *Phys. Rep.* **340** 291, eprint: astro-ph/9912508 (cit. on pp. 3, 9, 13).
- Battye, R. A. and A. Moss (2014), *Evidence for Massive Neutrinos from Cosmic Microwave Background and Lensing Observations*, *Physical Review Letters* **112**, 051303 051303, arXiv: 1308.5870 (cit. on p. 1).
- Blake, C. (2019), *Power spectrum modelling of galaxy and radio intensity maps including observational effects*, arXiv e-prints, arXiv: 1902.07439 (cit. on p. 1).
- Crittenden, R. G. et al. (2002), *Discriminating Weak Lensing from Intrinsic Spin Correlations Using the Curl-Gradient Decomposition*, *ApJ* **568** 20, eprint: astro-ph/0012336 (cit. on p. 1).
- Dyson, F. W., A. S. Eddington and C. Davidson (1920), *A Determination of the Deflection of Light by the Sun's Gravitational Field, from Observations Made at the Total Eclipse of May 29, 1919*, *Philosophical Transactions of the Royal Society of London Series A* **220** 291 (cit. on p. 10).
- Eke, V. R., S. Cole and C. S. Frenk (1996), *Cluster evolution as a diagnostic for Omega*, *MNRAS* **282**, eprint: astro-ph/9601088 (cit. on p. 8).
- Harnois-Déraps, J. et al. (2018), *Cosmological simulations for combined-probe analyses: covariance and neighbour-exclusion bias*, *MNRAS* **481** 1337, arXiv: 1805.04511 (cit. on p. 31).
- Heitmann, K. et al. (2014), *The Coyote Universe Extended: Precision Emulation of the Matter Power Spectrum*, *ApJ* **780**, 111 111, arXiv: 1304.7849 (cit. on p. 8).
- Heymans, C. et al. (2013), *CFHTLenS tomographic weak lensing cosmological parameter constraints: Mitigating the impact of intrinsic galaxy alignments*, *MNRAS* **432** 2433, arXiv: 1303.1808 (cit. on p. 1).
- Hikage, C. et al. (2019), *Cosmology from cosmic shear power spectra with Subaru Hyper Suprime-Cam first-year data*, *PASJ*, arXiv: 1809.09148 (cit. on p. 1).
- Hildebrandt, H. et al. (2017), *KiDS-450: cosmological parameter constraints from tomographic weak gravitational lensing*, *MNRAS* **465** 1454, arXiv: 1606.05338 (cit. on pp. 1, 2, 15, 19, 29, 41).
- Hildebrandt, H. et al. (2018), *KiDS+VIKING-450: Cosmic shear tomography with optical+infrared data*, arXiv e-prints, arXiv: 1812.06076 (cit. on pp. 1, 19, 32).
- Hubble, E. (1929), *A Relation between Distance and Radial Velocity among Extra-Galactic Nebulae*, *Contributions from the Mount Wilson Observatory*, vol. 3, pp.23-28 **3** 23 (cit. on p. 3).
- Kaiser, N. (1992), *Weak gravitational lensing of distant galaxies*, *ApJ* **388** 272 (cit. on pp. 13, 14).
- Kaiser, N. and G. Squires (1993), *Mapping the dark matter with weak gravitational lensing*, *ApJ* **404** 441 (cit. on p. 12).

- Köhlinger, F. et al. (2017), *KiDS-450: the tomographic weak lensing power spectrum and constraints on cosmological parameters*, *MNRAS* **471** 4412, arXiv: [1706.02892](#) (cit. on p. 31).
- Planck Collaboration et al. (2016), *Planck 2015 results. XIV. Dark energy and modified gravity*, *A&A* **594**, A14 A14, arXiv: [1502.01590](#) (cit. on p. 1).
- Planck Collaboration et al. (2018), *Planck 2018 results. VI. Cosmological parameters*, ArXiv e-prints, arXiv: [1807.06209](#) (cit. on pp. 1, 5, 8).
- Rich, J. (2001), *Fundamentals of Cosmology* (cit. on p. 8).
- Schneider, P. (2012), *Gravitational lensing – Lecture Notes* (cit. on p. 13).
- Schneider, P. (2015), *Extragalactic Astronomy and Cosmology: An Introduction* (cit. on pp. 3, 7, 11).
- Schneider, P., T. Eifler and E. Krause (2010), *COSEBIs: Extracting the full E-/B-mode information from cosmic shear correlation functions*, *A&A* **520**, A116 A116, arXiv: [1002.2136](#) (cit. on pp. 16, 24, 33).
- Schneider, P. and M. Kilbinger (2007), *The ring statistics - how to separate E- and B-modes of cosmic shear correlation functions on a finite interval*, *A&A* **462** 841, eprint: [astro-ph/0605084](#) (cit. on p. 16).
- Schneider, P., L. van Waerbeke and Y. Mellier (2002), *B-modes in cosmic shear from source redshift clustering*, *A&A* **389** 729, eprint: [astro-ph/0112441](#) (cit. on pp. 1, 16, 24).
- Schramm, T. and R. Kayser (1995), *The complex theory of gravitational lensing. Beltrami equation and cluster lensing.*, *A&A* **299** 1, eprint: [astro-ph/9408064](#) (cit. on p. 11).
- Seitz, C. and P. Schneider (1997), *Steps towards nonlinear cluster inversion through gravitational distortions. III. Including a redshift distribution of the sources.*, *A&A* **318** 687, eprint: [astro-ph/9601079](#) (cit. on p. 11).
- Seitz, S. and P. Schneider (2001), *A new finite-field mass reconstruction algorithm*, *A&A* **374** 740 (cit. on p. 12).
- Shirasaki, M. et al. (2019), *Mock galaxy shape catalogs in the Subaru Hyper Suprime-Cam Survey*, arXiv e-prints, arXiv: [1901.09488](#) (cit. on p. 1).
- Takahashi, R. et al. (2012), *Revising the Halofit Model for the Nonlinear Matter Power Spectrum*, *ApJ* **761**, 152 152, arXiv: [1208.2701](#) (cit. on pp. 8, 29).
- Troxel, M. A. et al. (2018), *Dark Energy Survey Year 1 results: Cosmological constraints from cosmic shear*, *Phys. Rev. D* **98**, 043528 043528, arXiv: [1708.01538](#) (cit. on p. 1).
- Van Waerbeke, L. et al. (2006), *Redshift and shear calibration: Impact on cosmic shear studies and survey design*, *Astroparticle Physics* **26** 91, eprint: [astro-ph/0603696](#) (cit. on pp. 28, 31).
- Verde, L., P. Protopapas and R. Jimenez (2013), *Planck and the local Universe: Quantifying the tension*, *Physics of the Dark Universe* **2** 166, arXiv: [1306.6766 \[astro-ph.CO\]](#) (cit. on p. 1).
- Wright, A. H. et al. (2018), *KiDS+VIKING-450: A new combined optical & near-IR dataset for cosmology and astrophysics*, arXiv e-prints, arXiv: [1812.06077](#) (cit. on p. 19).

Detailed calculations

A.1 Calculation of the power spectrum

In this Section we will perform the calculation for the observed power spectrum $P^{\text{obs}}(\ell)$. For this, we assume an infinitely large field in order to perform our integration over \mathbb{R}^2 . In reality, finite field effects would play a role here. We begin with the calculation of the correlation for the Fourier transformed shear:

$$\begin{aligned}
 & \langle \tilde{\gamma}^{\text{obs}}(\ell) \tilde{\gamma}^{\text{obs}*}(\ell') \rangle \\
 &= \left\langle \int d^2\theta \int d^2\theta' W(\theta) W(\theta') \gamma(\theta) \gamma^*(\theta') \exp(i\ell\theta - i\ell'\theta') \right\rangle \\
 &= \left\langle \int d^2\theta \int d^2\theta' W(\theta) W(\theta') \exp(i\ell\theta - i\ell'\theta') \int \frac{d^2k}{(2\pi)^2} \int \frac{d^2\ell}{(2\pi)^2} \tilde{\gamma}(\mathbf{k}) \tilde{\gamma}^*(\ell) \exp(-i\mathbf{k}\theta + i\ell\theta') \right\rangle \\
 &= \left\langle \int d^2\theta \int d^2\theta' \int \frac{d^2k}{(2\pi)^2} \int \frac{d^2\ell}{(2\pi)^2} P(\mathbf{k}) (2\pi)^2 \delta(\mathbf{k} - \ell) \exp[i(\ell\theta - \ell'\theta' - \mathbf{k}\theta + \ell\theta')] W(\theta) W(\theta') \right\rangle \\
 &= \left\langle \int \frac{d^2k}{(2\pi)^2} P(\mathbf{k}) \int d^2\theta W(\theta) \exp[i\theta(\ell - \mathbf{k})] \int d^2\theta' W(\theta') \exp[-i\theta'(\ell' - \mathbf{k})] \right\rangle \\
 &= \left\langle \int \frac{d^2k}{(2\pi)^2} P(\mathbf{k}) \tilde{W}(\ell - \mathbf{k}) \tilde{W}^*(\ell' - \mathbf{k}) \right\rangle \tag{A.1}
 \end{aligned}$$

It is important to keep in mind that the ensemble averages of the weight function are independent of the ensemble averages of the shear values, meaning $\langle W(\theta) \gamma(\theta) \rangle = \langle W(\theta) \rangle \langle \gamma(\theta) \rangle$. We can define

$W(\boldsymbol{\theta}) = 1 + w(\boldsymbol{\theta})$ with $\langle w(\boldsymbol{\theta}) \rangle = 0$, which leads to the expression

$$\begin{aligned}
 & \langle \tilde{\gamma}^{\text{obs}}(\boldsymbol{\ell}) \tilde{\gamma}^{\text{obs}*}(\boldsymbol{\ell}') \rangle \\
 &= \left\langle \int \frac{d^2 k}{(2\pi)^2} P(\mathbf{k}) \left[(2\pi)^4 \delta(\boldsymbol{\ell} - \mathbf{k}) \delta(\boldsymbol{\ell}' - \mathbf{k}) + (2\pi)^2 [\tilde{w}(\boldsymbol{\ell} - \mathbf{k}) \delta(\boldsymbol{\ell}' - \mathbf{k}) + \tilde{w}^*(\boldsymbol{\ell}' - \mathbf{k}) \delta(\boldsymbol{\ell} - \mathbf{k})] \right. \right. \\
 & \quad \left. \left. + \tilde{w}(\boldsymbol{\ell} - \mathbf{k}) \tilde{w}(\boldsymbol{\ell}' - \mathbf{k}) \right] \right\rangle \\
 &= (2\pi)^2 \delta(\boldsymbol{\ell} - \boldsymbol{\ell}') P(\boldsymbol{\ell}) + \left[\langle \tilde{w}(\boldsymbol{\ell} - \boldsymbol{\ell}') \rangle P(\boldsymbol{\ell}') + \langle \tilde{w}^*(\boldsymbol{\ell}' - \boldsymbol{\ell}) \rangle P(\boldsymbol{\ell}) \right] + \left\langle \int \frac{d^2 k}{(2\pi)^2} \tilde{w}(\boldsymbol{\ell} - \mathbf{k}) \tilde{w}^*(\boldsymbol{\ell}' - \mathbf{k}) P(\mathbf{k}) \right\rangle \\
 &\stackrel{(*)}{=} (2\pi)^2 \delta(\boldsymbol{\ell} - \boldsymbol{\ell}') P(\boldsymbol{\ell}) + \left\langle \int \frac{d^2 k}{(2\pi)^2} \tilde{w}(\boldsymbol{\ell} - \mathbf{k}) \tilde{w}^*(\boldsymbol{\ell}' - \mathbf{k}) P(\mathbf{k}) \right\rangle, \tag{A.2}
 \end{aligned}$$

where in (*) we have used that the average $\langle \tilde{w}(\boldsymbol{\ell}) \rangle$ vanishes. Up until now, we have not specified our weight-function w . We parametrize it as

$$w(\boldsymbol{\theta}) = \sum_{\boldsymbol{\alpha} \in \mathbb{Z}^2} w_{\boldsymbol{\alpha}} \Xi(\boldsymbol{\theta} - L\boldsymbol{\alpha}), \text{ with the Box-Function } \Xi(\boldsymbol{\theta}) = \begin{cases} 1 & \boldsymbol{\theta} \in \left[-\frac{L}{2}, \frac{L}{2}\right]^2 \\ 0 & \text{else} \end{cases}. \tag{A.3}$$

Here, the $w_{\boldsymbol{\alpha}}$ are random variables, drawn from the random distribution describing the survey depths. For the Fourier-Transform we compute:

$$\tilde{w}(\boldsymbol{\ell}) = \sum_{\boldsymbol{\alpha} \in \mathbb{Z}^2} w_{\boldsymbol{\alpha}} \exp(-i\boldsymbol{\ell} L \boldsymbol{\alpha}) \tilde{\Xi}(\boldsymbol{\ell}), \tag{A.4}$$

where

$$\tilde{\Xi}(\boldsymbol{\ell}) = \frac{4 \sin\left(\frac{L\ell_1}{2}\right) \sin\left(\frac{L\ell_2}{2}\right)}{\ell_1 \ell_2}, \tag{A.5}$$

is a 2-dimensional sinc function. Assuming an uncorrelated weight-distribution ($\langle w_{\boldsymbol{\alpha}} w_{\boldsymbol{\beta}} \rangle = 0$ for $\boldsymbol{\alpha} \neq \boldsymbol{\beta}$) and setting $\langle w^2 \rangle \equiv \langle w_{\boldsymbol{\alpha}}^2 \rangle$ for each $\boldsymbol{\alpha}$, we get

$$\begin{aligned}
 & \left\langle \int \frac{d^2 k}{(2\pi)^2} \tilde{w}(\boldsymbol{\ell} - \mathbf{k}) \tilde{w}^*(\boldsymbol{\ell}' - \mathbf{k}) P(\mathbf{k}) \right\rangle \\
 &= \left\langle \int \frac{d^2 k}{(2\pi)^2} \sum_{\boldsymbol{\alpha}, \boldsymbol{\beta}} w_{\boldsymbol{\alpha}} w_{\boldsymbol{\beta}} \exp[-i(\boldsymbol{\ell} - \mathbf{k}) L \boldsymbol{\alpha}] \tilde{\Xi}(\boldsymbol{\ell} - \mathbf{k}) \exp[i(\boldsymbol{\ell}' - \mathbf{k}) L \boldsymbol{\beta}] \tilde{\Xi}^*(\boldsymbol{\ell}' - \mathbf{k}) P(\mathbf{k}) \right\rangle \\
 &= \int \frac{d^2 k}{(2\pi)^2} \sum_{\boldsymbol{\alpha}} \langle w^2 \rangle \exp[-i(\boldsymbol{\ell} - \mathbf{k}) L \boldsymbol{\alpha} + i(\boldsymbol{\ell}' - \mathbf{k}) L \boldsymbol{\alpha}] \tilde{\Xi}(\boldsymbol{\ell} - \mathbf{k}) \tilde{\Xi}^*(\boldsymbol{\ell}' - \mathbf{k}) P(\mathbf{k}). \tag{A.6}
 \end{aligned}$$

Using this result, we can obtain the observed power spectrum

$$P^{\text{obs}}(\boldsymbol{\ell}) = \frac{1}{(2\pi)^2} \int d^2 \ell' \langle \tilde{\gamma}^{\text{obs}}(\boldsymbol{\ell}) \tilde{\gamma}^{\text{obs}*}(\boldsymbol{\ell}') \rangle, \tag{A.7}$$

by performing the ℓ' -integration in (A.2):

$$\begin{aligned}
 P^{\text{obs}}(\ell) &= P(\ell) + \int \frac{d^2 \ell'}{(2\pi)^2} \int \frac{d^2 k}{(2\pi)^2} \sum_{\alpha} \langle w^2 \rangle \exp[-i(\ell - k)L\alpha + i(\ell' - k)L\alpha] \tilde{\Xi}(\ell - k) \tilde{\Xi}(\ell' - k) P(k) \\
 &= P(\ell) + \int \frac{d^2 k}{(2\pi)^2} \sum_{\alpha} \langle w^2 \rangle \exp[-i(\ell - k)L\alpha] \tilde{\Xi}(\ell - k) P(k) \int \frac{d^2 \ell'}{(2\pi)^2} \tilde{\Xi}^*(\ell' - k) \exp[i(\ell' - k)L\alpha] \\
 &= P(\ell) + \langle w^2 \rangle \int \frac{d^2 k}{(2\pi)^2} \tilde{\Xi}(\ell - k) P(k) \sum_{\alpha} \exp[-i(\ell - k)L\alpha] \Xi(L\alpha) \\
 &= P(\ell) + \langle w^2 \rangle \int \frac{d^2 k}{(2\pi)^2} \tilde{\Xi}(\ell - k) P(k), \tag{A.8}
 \end{aligned}$$

which is a convolution of the power spectrum and the 2-dimensional sinc function.

A.2 Calculation of the shear correlation functions

Following Hildebrandt et al. (2017), given a set of galaxies we calculate the shear correlation functions via

$$\xi_+^{ij}(\theta) = \frac{\sum_{a,b} w_a^i w_b^j \epsilon_a^i \epsilon_b^{j*} \Delta(|\theta_a^i - \theta_b^j|)}{\sum_{a,b} w_a^i w_b^j \Delta(|\theta_a^i - \theta_b^j|)}. \tag{A.9}$$

Here, w represents the lensing weight of the galaxy, whereas ϵ is its (complex) ellipticity and θ its position on the sky. We have defined the function Δ as

$$\Delta(|\theta_a^i - \theta_b^j|) = \begin{cases} 1, & |\theta_a^i - \theta_b^j| \in [\theta, \theta + d\theta] \\ 0, & \text{else} \end{cases}, \tag{A.10}$$

where we assume $d\theta \ll \theta$. We define N as the number of pointings in the survey and F_k^i as the set of galaxies in pointing k and tomographic bin i . The numerator in Equation (A.9) then transforms to:

$$\begin{aligned}
 & \sum_{k,\ell=1}^N \sum_{a \in F_k^i} \sum_{b \in F_\ell^j} w_a^i w_b^j \epsilon_a^i \epsilon_b^{j*} \Delta(|\theta_a^i - \theta_b^j|) \\
 &= \sum_{k=1}^N \sum_{a \in F_k^i} w_a^i \sum_{\ell=1}^N \sum_{b \in F_\ell^j} w_b^j \Delta(|\theta_a^i - \theta_b^j|) \epsilon_a^i \epsilon_b^{j*} \\
 &= \sum_{k=1}^N \sum_{a \in F_k^i} w_a^i \left[\sum_{b \in F_k^j} w_b^j \Delta(|\theta_a^i - \theta_b^j|) \epsilon_a^i \epsilon_b^{j*} + \sum_{\ell \neq k} \sum_{b \in F_\ell^j} w_b^j \Delta(|\theta_a^i - \theta_b^j|) \epsilon_a^i \epsilon_b^{j*} \right]. \tag{A.11}
 \end{aligned}$$

When we denote the probability that pointing k is of percentile m by P_m^k and assume that the product $\epsilon_a^i \epsilon_b^{j*}$ always equals its expectation value, we can set the numerator as

$$\sum_{k=1}^N \sum_{a \in F_k^i} w_a^i \sum_m P_m^k \left[\overbrace{\sum_{b \in F_k^j} w_b^j \Delta(|\theta_a^i - \theta_b^j|)}^{(A.12.a)} \xi_{+,mm}^{ij}(\theta) + \overbrace{\sum_{\ell \neq k} \sum_{b \in F_\ell^j} w_b^j \Delta(|\theta_a^i - \theta_b^j|)}^{(A.12.b)} \sum_n P_n^\ell \xi_{+,mn}^{ij}(\theta) \right]. \quad (A.12)$$

The term (A.12.a) denotes all galaxies that lie within distance interval $[\theta, \theta + d\theta]$ of galaxy a , and are in the same pointing as galaxy a . This term is equal to the (weighted) number density of galaxies in the pointing multiplied by $2\pi\theta d\theta E(\theta)$.

The term (A.12.b) denotes all galaxies within distance interval $[\theta, \theta + d\theta]$ of galaxy a , that are *not* in the same pointing as galaxy a . This is equal to the number density of galaxies in the respective pointings multiplied by $2\pi\theta d\theta [1 - E(\theta)]$.

If we assume that said number density in a pointing is equal to the number density in the percentile it belongs to, N_n^j , and set $P_n^\ell = 1/10$, the numerator becomes

$$\sum_{k=1}^N \sum_{a \in F_k^i} w_a^i \sum_m P_m^k \left[2\pi\theta d\theta E(\theta) N_m^j \xi_{+,mm}^{ij}(\theta) + 2\pi\theta d\theta \frac{1 - E(\theta)}{10} \sum_n N_n^j \xi_{+,mn}^{ij}(\theta) \right]. \quad (A.13)$$

Now the term $\sum_{a \in F_k^i} w_a^i$ denotes the (weighted) number of galaxies in pointing k , which we set as the number density of galaxies in the respective percentile multiplied with the area A of the pointing. Applying this and setting $P_m^k = 1/10$, the numerator reads

$$\begin{aligned} & \frac{2\pi\theta d\theta}{10} \sum_{k=1}^N \sum_m N_m^i A \left[E(\theta) N_m^j \xi_{+,mm}^{ij}(\theta) + \frac{1 - E(\theta)}{10} \sum_n N_n^j \xi_{+,mn}^{ij}(\theta) \right] \\ &= \frac{2\pi\theta d\theta NA}{10} \sum_m N_m^i \left[E(\theta) N_m^j \xi_{+,mm}^{ij}(\theta) + \frac{1 - E(\theta)}{10} \sum_n N_n^j \xi_{+,mn}^{ij}(\theta) \right]. \end{aligned} \quad (A.14)$$

The same line of argumentation can be applied to the denominator, which then reads:

$$\frac{2\pi\theta d\theta NA}{10} \sum_m N_m^i \left[E(\theta) N_m^j + \frac{1 - E(\theta)}{10} \sum_n N_n^j \right]. \quad (A.15)$$

Taking the ratio of the two quantities, we see that Equations (A.9) and (3.20) are the same¹.

¹ Note that while here N_m^i denotes a number density, in Equations (A.9) and (3.20) it denotes the total (weighted) number of galaxies. However, the difference is just a multiplication with the area A of the pointings, which appears both in the numerator and the denominator and is thus cancelled out.

Outlook: Finite field effects

In this chapter we will outline how to calculate the correction of the correlation functions for a finite survey with a potentially correlated distribution of depth between pointings. Essentially, this boils down to the calculation of $P_{mn}^{ij}(\theta)$ from Equation (3.16). We calculate this weighting by the geometrical probability that a pair of galaxies of separation θ is of percentiles m and n , $P(m, n|\theta)$, weighted by the respective number of galaxies in the percentiles N_m^i, N_n^j :

$$P_{mn}^{ij}(\theta) = N_m^i N_n^j P(m, n|\theta). \quad (\text{B.1})$$

At first we define Functions $E_{ab}(\theta)$ as the probability that a galaxy pair of separation θ is in pointings of distance (a, b) . This situation is depicted in Figure B.1. Due to symmetry, for the azimuthal average of the functions, $E_{ab}(\theta) = E_{-ab}(\theta) = E_{ba}(\theta)$ holds for all combinations of a and b . Note that $E_{00}(\theta) = E(\theta)$ and $\sum_{a,b} E_{ab}(\theta) \equiv 1$.

Let $P^*(m, n|a, b)$ denote the probability that two pointings of distance (a, b) are of percentile m and n (which is directly calculable from a given survey footprint). Then the following equation holds:

$$P(m, n|\theta) = \sum_{a,b} E_{ab}(\theta) P^*(m, n|a, b). \quad (\text{B.2})$$

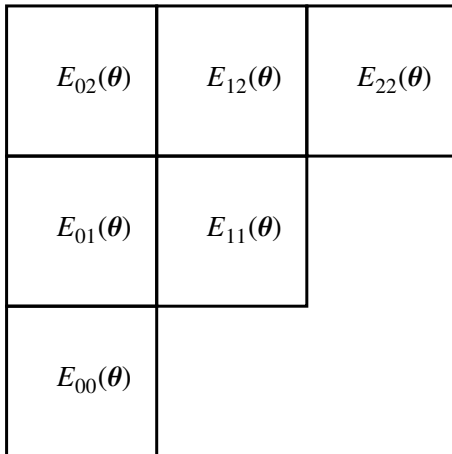


Figure B.1 – Graphic representation of the definitions of $E_{ab}(\theta)$. When the first galaxy is in the bottom left pointing, the probability to find the second galaxy in a pointing of distance (a, b) is $E_{mn}(\theta)$.

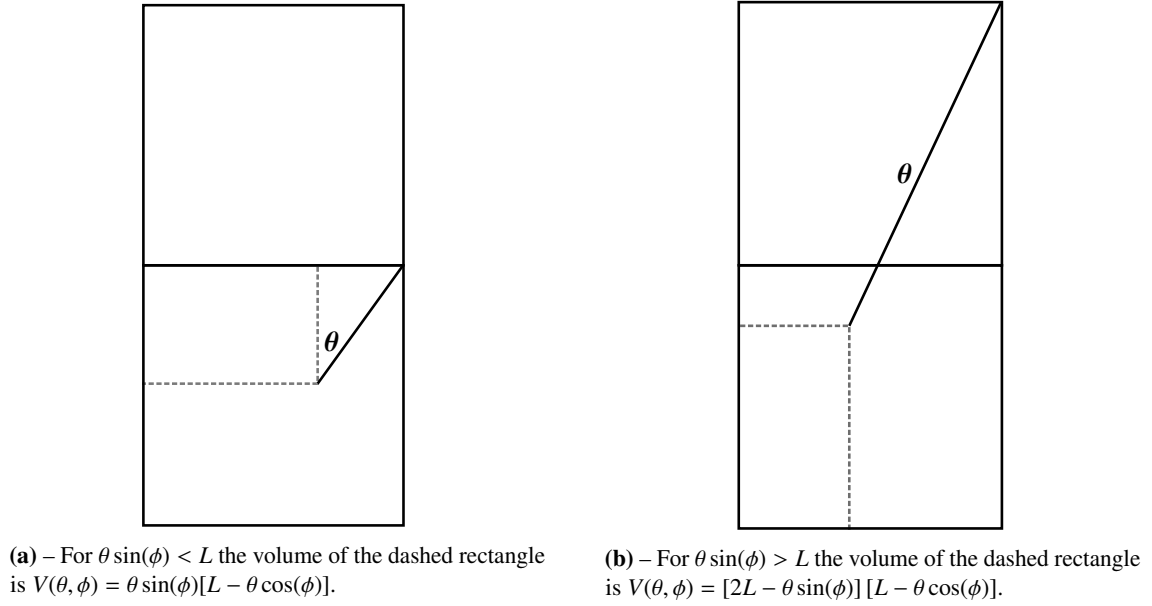


Figure B.2 – How to calculate $E_{01}(\theta)$ for different values of θ .

Note that the expectation value of $P^*(m, n|a, b)$ for uncorrelated distributions is

$$\langle P^*(m, n|a, b) \rangle = \begin{cases} 0.1 \delta_{mn}, & \text{for } (a, b) = (0, 0) \\ 0.01, & \text{else} \end{cases}, \quad (\text{B.3})$$

where δ_{mn} denotes the Kronecker delta. Keeping in mind that

$$\sum_{(a,b) \neq (0,0)} E_{ab}(\theta) = 1 - E(\theta), \quad (\text{B.4})$$

we can use the expectation value (B.3) to calculate (B.2) as a consistency check. In that case, we receive the same value for the coefficients in (B.1) as we have in Equation (3.19) in Chapter 3.2 for the case of an infinite footprint and uncorrelated distribution of depth.

The E_{ab} can all be calculated analytically, similar to our method in Chapter 3.1.3. We again assume a selection of square fields with side length L , and later set $L = 60'$ to adapt to the KV450 survey. As an example, for E_{01} we have several possible situations, depicted in Figure B.2. For a separation vector θ with modulus $\theta < L$ and inclination angle ϕ , the dashed rectangle in Figure B.2(a) depicts the galaxies that have a partner in the upper pointing. For $L < \theta < \sqrt{2}L$, the dashed rectangle in Figure B.2(a) represents the area of galaxies with a partner in the upper square under the condition that $\theta \sin(\phi) < L$. For $\theta \sin(\phi) > L$, the situation is depicted by Figure B.2(b). As soon as $\theta > \sqrt{2}L$ holds, the situation of Figure B.2(a) is impossible. When $\theta < 2L$ holds, the vector is only constrained by $\theta \cos(\phi) < L$, but as soon as $\theta > 2L$ holds, we additionally need to impose $\theta \sin(\phi) < 2L$. Again setting $E_{ab}(\theta) = V(\theta, \phi)/L^2$, we define

$$\begin{aligned} E_{01}^{(a)}(\theta) &\equiv \frac{\theta}{L} \sin(\phi) \left[1 - \frac{\theta}{L} \cos(\phi) \right] \\ E_{01}^{(b)}(\theta) &\equiv \left[2 - \frac{\theta}{L} \sin(\phi) \right] \left[1 - \frac{\theta}{L} \cos(\phi) \right] \end{aligned} \quad (\text{B.5})$$

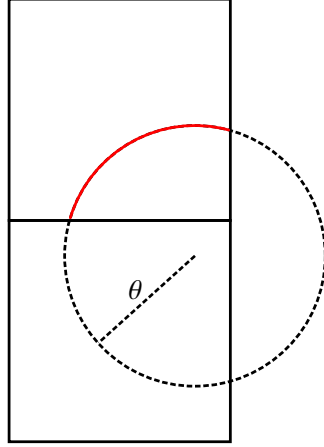


Figure B.3 – Visualisation of the numerical computation for $E_{01}(\theta)$. For a circle of radius θ , the length of the red arc divided by 2π represents the fraction of galaxies within the respective pointing. This value needs to be integrated for all possible centers of the circle in the pointing. That procedure is straightforward to expand for other $E_{ab}(\theta)$.

Taking the azimuthal average, we compute:

$$E_{01}(\theta) = \begin{cases} \frac{1}{\pi} \int_0^{\frac{\pi}{2}} d\phi E_{01}^{(a)}(\theta) & \frac{\theta}{L} < 1 \\ \frac{1}{\pi} \left[\int_{\cos^{-1}(L/\theta)}^{\sin^{-1}(L/\theta)} d\phi E_{01}^{(a)}(\theta) + \int_{\sin^{-1}(L/\theta)}^{\frac{\pi}{2}} d\phi E_{01}^{(b)}(\theta) \right] & 1 < \frac{\theta}{L} < \sqrt{2} \\ \frac{1}{\pi} \int_{\cos^{-1}(L/\theta)}^{\frac{\pi}{2}} d\phi E_{01}^{(b)}(\theta) & \sqrt{2} < \frac{\theta}{L} < 2 \\ \frac{1}{\pi} \int_{\cos^{-1}(L/\theta)}^{\sin^{-1}(2L/\theta)} d\phi E_{01}^{(b)}(\theta) & 2 < \frac{\theta}{L} < \sqrt{5} \\ 0 & \sqrt{5} < \frac{\theta}{L} \end{cases}$$

$$= \begin{cases} \frac{(2L-\theta)\theta}{2\pi L^2} & \frac{\theta}{L} < 1 \\ \frac{1}{\pi} \left[\frac{3}{2} - 2\frac{\theta}{L} + \frac{\theta^2}{L^2} + 2\sqrt{\frac{\theta^2}{L^2} - 1} + 2\sec^{-1}\left(\frac{\theta}{L}\right) \right] & 1 < \frac{\theta}{L} < \sqrt{2} \\ \frac{1}{2\pi} \left[-1 - 4\frac{\theta}{L} + 4\sqrt{\frac{\theta^2}{L^2} - 1} + 4\csc^{-1}\left(\frac{\theta}{L}\right) \right] & \sqrt{2} < \frac{\theta}{L} < 2 \\ \frac{1}{2\pi} \left[-5 - \frac{\theta^2}{L^2} + 2\sqrt{\frac{\theta^2}{L^2} - 4} + 4\sqrt{\frac{\theta^2}{L^2} - 1} - 4\sec^{-1}\left(\frac{\theta}{L}\right) + 4\sin^{-1}\left(\frac{2L}{\theta}\right) \right] & 2 < \frac{\theta}{L} < \sqrt{5} \\ 0 & \sqrt{5} < \frac{\theta}{L} \end{cases} \quad (\text{B.6})$$

Naturally, to calculate those functions for all possible combinations would be rather tedious, however they are simple to determine numerically (compare Figure B.3). A plot of these functions can be found in Figure B.4.

When we now simulate random distributions of the depth-function for a 100 deg^2 -field, a 450 deg^2 -field and a 1000 deg^2 -field, we can compare how they differ from each other and estimate how important finite-field effects are. As can be seen from Figures C.3, C.4 and C.5, the effect is quite significant for a 100 deg^2 -field, but almost negligible for a 1000 deg^2 -field. This leads to the assumption that both for the KiDS- as for the Euclid-survey, finite field effects do not need to be accounted for. However, if the distribution of depth is correlated in the surveys, that might have a noticeable impact on the results.

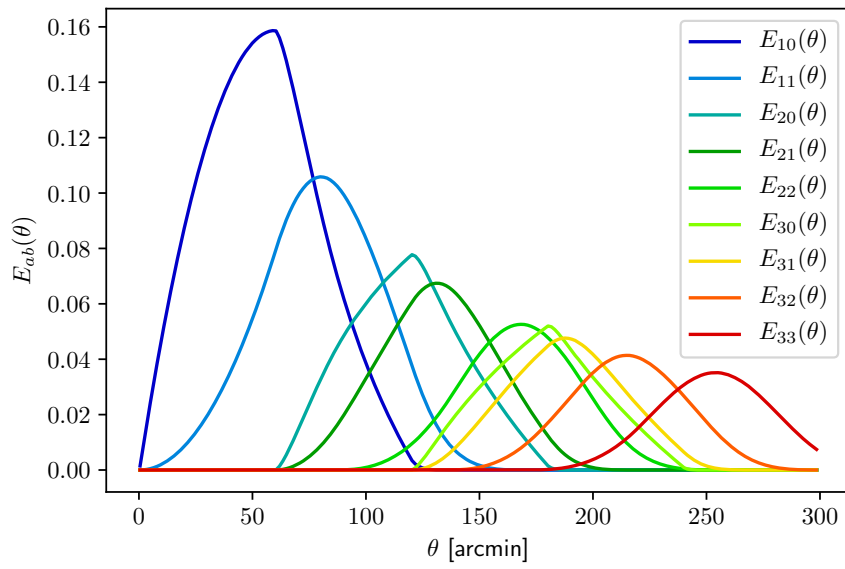


Figure B.4 – The functions $E_{ab}(\theta)$ for the first few possible combinations.

Additional figures and fables

C.1 Additional tables

Table C.1 – Weighted number of galaxies N and average redshift $\langle z \rangle$ for each percentile of each bin.

Percentile	Bin 1		Bin 2		Bin 3		Bin 4		Bin 5	
	$\langle z \rangle$	N	$\langle z \rangle$	N	$\langle z \rangle$	N	$\langle z \rangle$	N	$\langle z \rangle$	N
1	0.36	33230	0.45	45630	0.59	57873	0.78	33053	0.94	23633
2	0.40	37848	0.48	52642	0.62	69929	0.80	44464	0.97	31352
3	0.42	38410	0.49	56986	0.64	74411	0.81	47164	0.97	34352
4	0.44	37445	0.50	54066	0.66	75132	0.82	46911	0.98	34788
5	0.46	38698	0.52	57357	0.67	75679	0.83	49620	0.99	39126
6	0.49	40742	0.54	55456	0.69	82209	0.84	53458	0.99	42326
7	0.51	38417	0.55	56883	0.70	80228	0.85	54378	1.01	44319
8	0.51	40110	0.56	60966	0.72	91835	0.86	63515	1.01	49094
9	0.59	39655	0.59	59207	0.75	87330	0.86	59674	1.02	53566
10	0.63	41653	0.62	64526	0.80	104866	0.89	79990	1.04	63426

C.2 Results of the MCMC

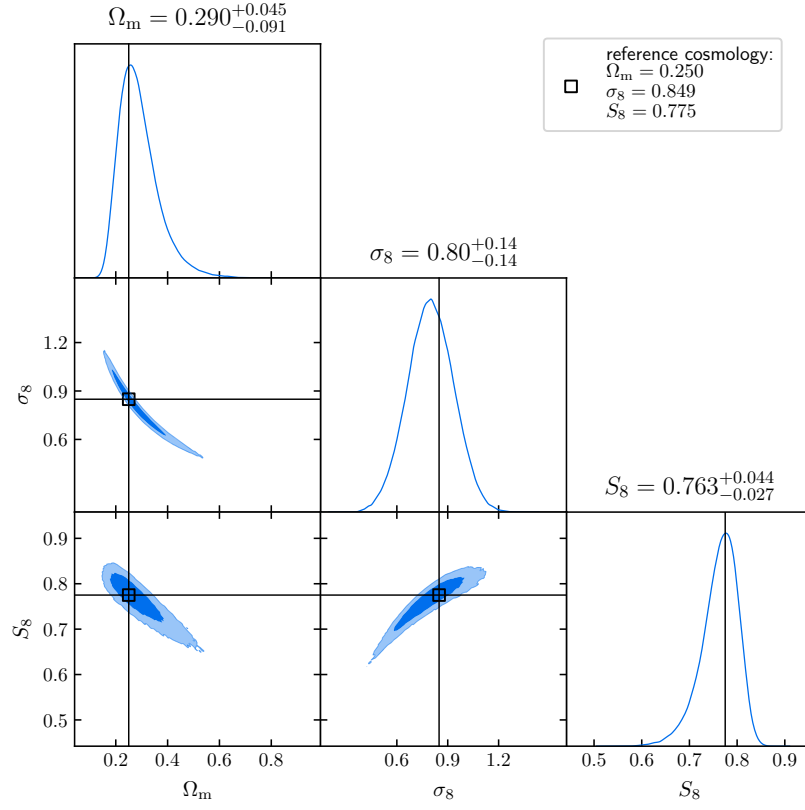


Figure C.1 – Bias in the parameters for a KiDS-like Survey.

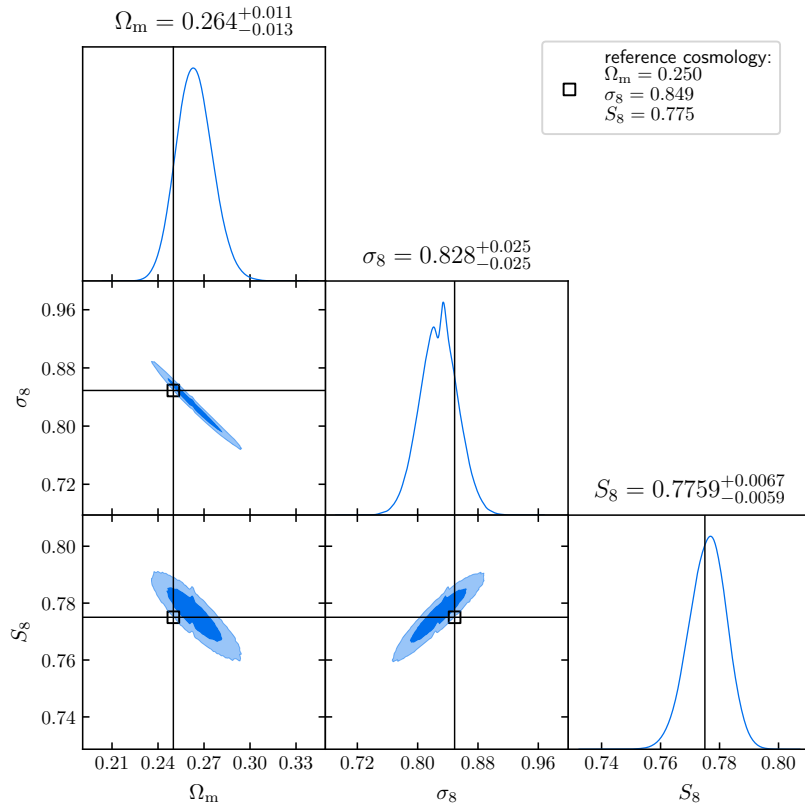


Figure C.2 – Bias in the parameters for a Euclid-like Survey.

C.3 Finite field effects

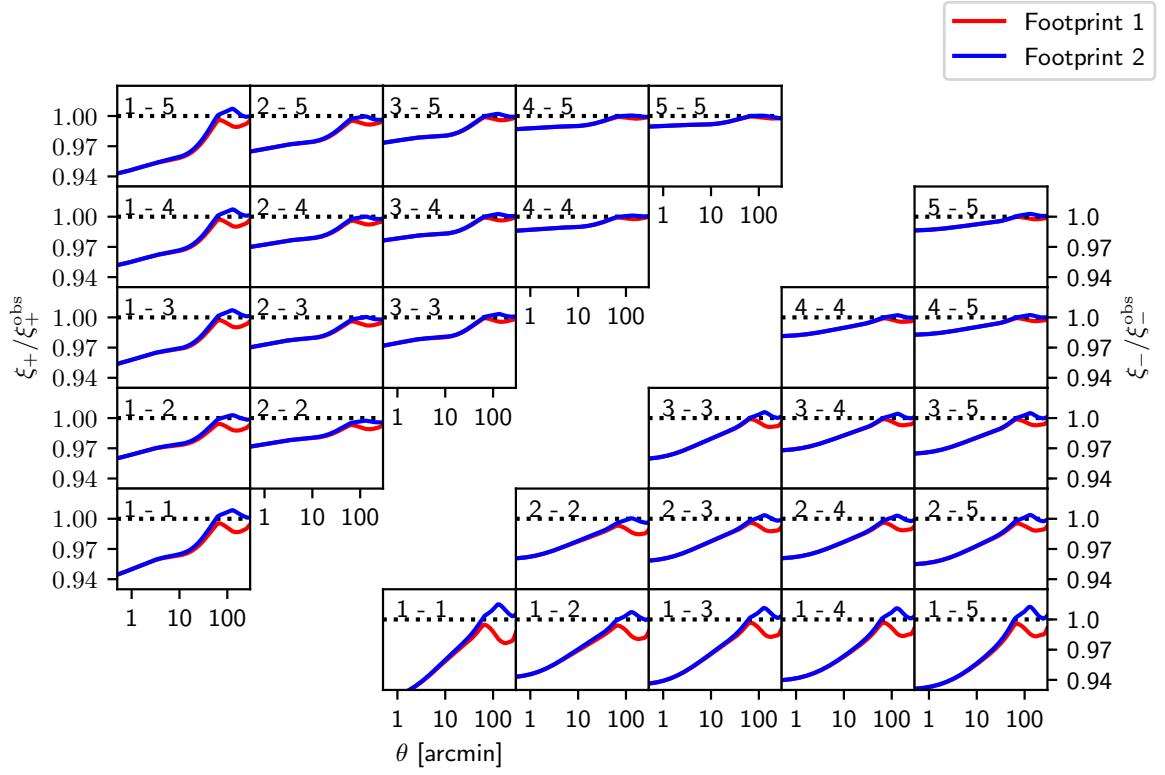


Figure C.3 – Correction of the correlation functions for two different distributions of percentiles for a 100 deg^2 -field.

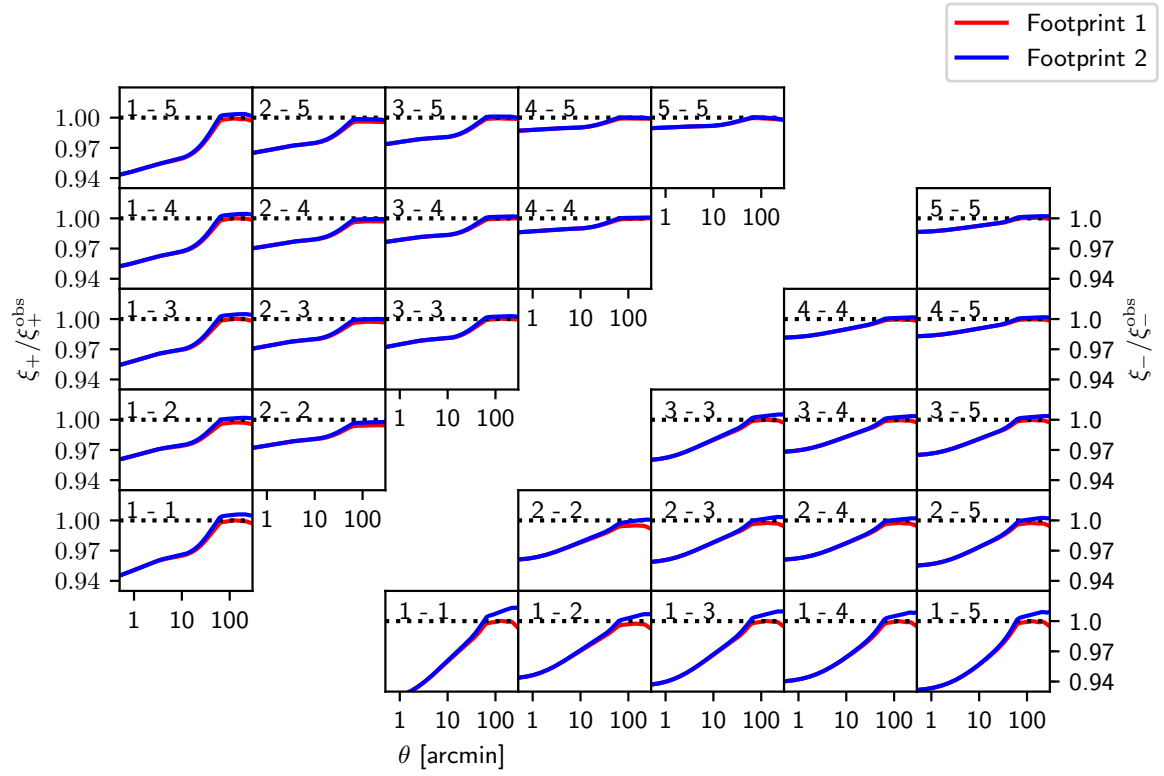


Figure C.4 – Correction of the correlation functions for two different distributions of percentiles for a 450 deg^2 -field.

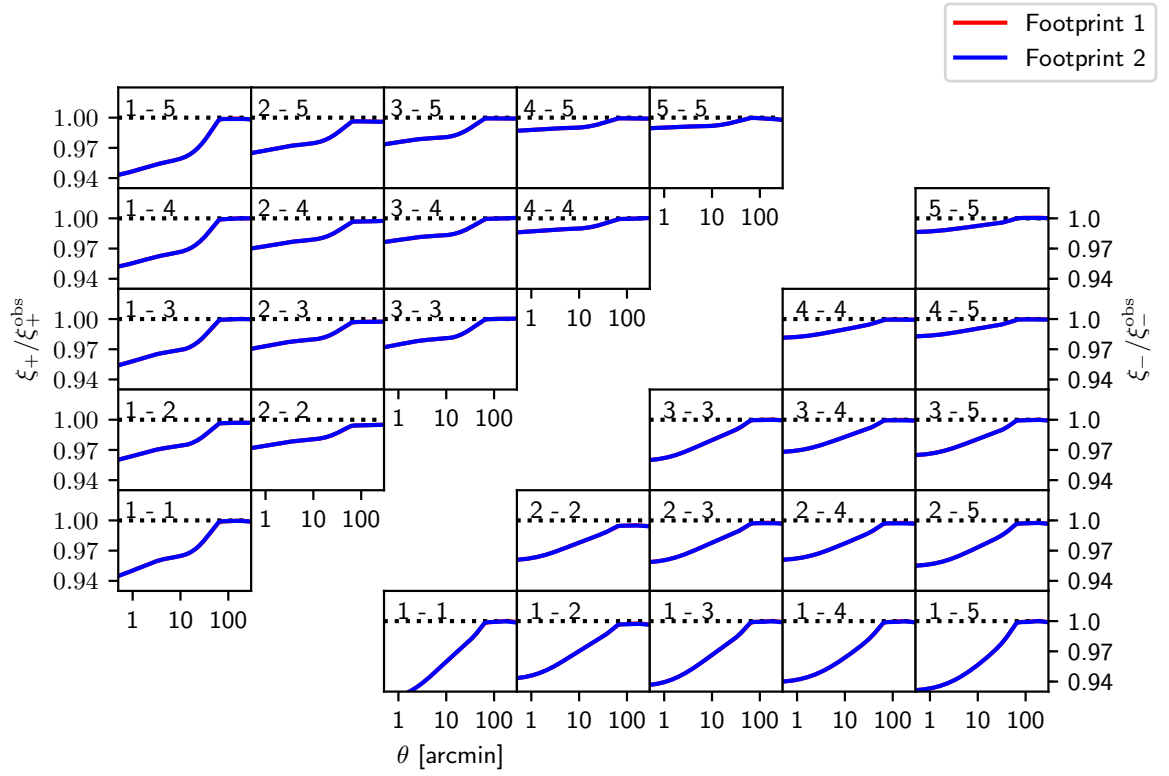


Figure C.5 – Correction of the correlation functions for two different distributions of percentiles for a 1000 deg²-field.

List of Figures

2.1	Sketch of a gravitational lensing event	9
2.2	Tangential and cross components of the shear for a galaxy.	13
2.3	Bessel Functions	14
3.1	Redshift distribution for the worst, a medium and the best percentile	20
3.2	Weighted number of galaxies as a function of redshift	21
3.3	Estimating E- and B-modes of a reconstructed convergence field.	23
3.4	B-mode power spectra in Gaussian random fields	25
3.5	Graphic how to obtain $E(\theta)$	25
3.6	Probability that a random pair of galaxies of separation θ lie in the same pointing. . . .	26
4.1	The ratio of modelled to observed correlation functions	32
4.2	E- and B-modes of the reference and the observed correlation functions	33
4.3	Difference in E- and B-modes between the reference and the observed correlation functions	34
B.1	Graphic how to obtain $E_{ab}(\theta)$	43
B.2	How to calculate $E_{01}(\theta)$	44
B.3	Visualisation of the numerical computation for $E_{01}(\theta)$	45
B.4	The functions $E_{ab}(\theta)$ for the first few possible combinations.	46
C.1	Bias in the parameters for a KiDS-like Survey.	48
C.2	Bias in the parameters for a Euclid-like Survey.	49
C.3	Correction of the correlation functions for a 100 deg^2 -field.	50
C.4	Correction of the correlation functions for a 450 deg^2 -field.	51
C.5	Correction of the correlation functions for a 1000 deg^2 -field.	52

List of Tables

3.1	Properties of the tomographic redshift bins in the KV450 Survey.	19
4.1	Parameter constraints from the MCMC simulations	33
C.1	Weighted number of galaxies N and average redshift $\langle z \rangle$ for each percentile of each bin.	47